Diploma Thesis

Hydrate failure in ITZ governs elastic limits of concrete subjected to multiaxial compressive loading

submitted in satisfaction of the requirements for the degree of
Diplom-Ingenieur
of the TU Wien, Department of Civil Engineering

Diplomarbeit

Hydratversagen in der ITZ führt zu Elastizitätsgrenzen von Beton unter mehraxialer Druckbelastung

ausgeführt zum Zwecke der Erlangung des akademischen Grades eines
Diplom-Ingenieurs
eingereicht an der Technischen Universität Wien, Fakultät für Bauingenieurwesen

von

Michael Schwaighofer, BSc

Matr.Nr.: 01225505

unter der Anleitung von

Univ.-Prof. Dipl.-Ing. Dr.techn. **Bernhard Pichler**

Dipl.-Ing. Dr.techn. **Markus Königsberger**, BSc

Institut für Mechanik der Werkstoffe und Strukturen
Technische Universität Wien
Karlsplatz 13/202, 1040 Wien, Österreich

Wien, im April 2021

Danksagung

An dieser Stelle möchte ich meinen beiden Betreuern dieser Diplomarbeit für Ihre tatkräftige Unterstützung danken. Besonders bedanken möchte ich bei Herrn Dipl.-Ing. Dr.techn. Markus Königsberger, BSc für die Einführung in die Materie der Mikromechanik, die Hilfe bei der Berechnung, sowie die vielen Erklärungen und Hinweise zur Erstellung der Diplomarbeit. Herrn Univ.-Prof. Dipl.-Ing. Dr.techn. Bernhard Pichler danke ich für die richtungsweisenden Anmerkungen während der gesamten Arbeit und die ausführlich erläuterten Korrekturen, durch die ich viel über das wissenschaftliche Schreiben gelernt habe. Ich konnte während meiner Arbeit viel von beiden Betreuern lernen, wofür ich Ihnen sehr dankbar bin.

Des Weiteren möchte ich mich bei meiner Familie für ihre Unterstützung während des Studiums bedanken. Besonderer Dank gebührt meiner Freundin, die mich mit Ihren Englisch-Kenntnissen beim Schreiben der Diplomarbeit unterstützte.

Abstract

Many concrete structures such as slabs, plates, shells, and arch dams are subjected to multiaxial loading. Of particular interest for engineers is the serviceability limit state (SLS) of these structures: the stress experienced by concrete must remain, under characteristic design loads, below the elastic limit of the material.

Herein, the elastic limits of concrete under multiaxial compression are investigated by means of a micromechanics multiscale model. Concrete is represented by three representative volume elements (RVEs), resolving the microstructural features of the material at three scales of observation. At the micrometer-scale, isotropically oriented, needle-shaped hydration products and capillary pores are considered to be in mutual interaction to form the RVE of "hydrate foam". At the millimeter-scale, this hydrate foam is considered as a matrix phase hosting unreacted clinker grains to form the RVE of "cement paste". Finally, the RVE of "concrete" at the centimeter-scale, consists of aggregates embedded in a cement paste matrix. Interfacial transition zones (ITZs), i.e. cement paste regions adjacent to the aggregate surfaces are most susceptible to microcracking. Hence, the elastic limits of multiaxially compressed concrete is considered to be reached when the most heavily loaded hydrate needle within the most unfavorable loaded ITZ fails according to a Drucker-Prager failure criterion. Composition and maturity of the concretes is considered by means of volume fractions of the constituents, computed according to Powers' hydration model.

Model-predicted elastic limits are compared to stress-strain diagrams from triaxial compression tests with axial symmetry or proportionally loaded multiaxial compression tests, as collected from six test campaigns reported in the literature on mature concretes with different compositions. The good agreement of model-predicted elastic limits with the initiation of major pre-peak nonlinearities in the experimentally determined stress-strain diagrams corroborates the importance of stress concentrations into ITZs and motivates the analysis of elastic limit surfaces in principal stress space, including sensitivity analysis. This reveals that (i) the aggregate-to-cement ratio has little influence on the elastic limit, (ii) the elastic limit decreases significantly with increasing water-to-cement ratio (w/c), at least in the regime $w/c > 0.42$, and (iii) the elastic limit increases with increasing hydration degree. Only for mature concretes and/or concretes with small w/c ratio, an increase of lateral confinement pressure increases the elastic limit significantly, whereas for young concretes and/or concretes with high w/c ratio, benefits due to confinement are rather limited. Finally, comparing the model-predicted elastic limit with the strength values from triaxial compression tests indicates (i) that the strength increases much more significantly with increasing confinement pressure than the elastic limit does, and (ii) that inelastic reserves

increase with increasing w/c ratios, as a consequence of the enhanced ability of inelastic material compaction resulting from the increased porosity.

Kurzfassung

Viele Betonbauwerke, wie etwa Scheiben, Platten, Schalen und Talsperren sind mehraxial beansprucht. Der Grenzzustand der Gebrauchstauglichkeit (SLS) ist für die Bemessung relevant: Die Spannungen von Beton müssen unter charakteristischen Bemessungslasten unterhalb der Elastizitätsgrenze des Materials bleiben.

In dieser Arbeit werden die Elastizitätsgrenzen für Beton unter mehraxialer Druckbeanspruchung mit einem Mehrskalen-Mikromechanik-Modell untersucht. Es basiert auf drei repräsentativen Volumenelementen (RVEs), die die Betonmikrostruktur auf drei Beobachtungsskalen darstellen. Auf der Mikrometerskala werden isotrop orientierte, nadelförmige Hydratationsprodukte und Kapillarporen in direkter gegenseitiger Interaktion eingeführt, um das RVE des „Hydratschaums“ zu definieren. Auf der Millimeterskala wird dieser Hydratschaum als Matrixphase berücksichtigt, die unhydrierte Klinkerkörner enthält, um das RVE des „Zementsteins“ zu bilden. Das RVE von „Beton“ auf der Zentimeterskala besteht aus Zuschlägen, die in einer Zementsteinmatrix eingebettet sind. Die „Interfacial Transition Zones“ (ITZs), also jene Zonen des Zementsteins, die direkt an die Zuschlagsoberflächen angrenzen, sind der Ausgangspunkt materieller Nichtlinearitäten, denn erste Mikrorissen treten genau dort auf. Daher wird die Elastizitätsgrenze von mehraxial druckbeanspruchtem Beton als erreicht angesehen, wenn die am stärksten belastete Hydratnadel innerhalb der am ungünstigsten belasteten ITZ gemäß des Drucker-Prager-Versagenskriteriums versagt. Die Zusammensetzungen und Hydratationsgrade der Betone werden mit Hilfe von Volumenanteilen der Materialbestandteile berücksichtigt, die mit dem Hydratationsmodell nach Powers berechnet werden.

Die vom Modell vorhergesagten Elastizitätsgrenzen werden mit Spannungs-Dehnungs-Diagrammen aus dreiaxialen Druckversuchen mit axialer Symmetrie oder proportional belasteten mehraxialen Druckversuchen verglichen, welche von sechs in der Literatur beschriebenen Versuchskampagnen für ausgehärtete Betone mit verschiedenen Zusammensetzungen stammen. Die gute Übereinstimmung der prognostizierten Elastizitätsgrenzen mit dem Beginn von wesentlichen Nichtlinearitäten in den experimentell ermittelten Spannungs-Dehnungs-Diagrammen untermauert die Bedeutung von Spannungskonzentrationen in ITZs und regt zu Analysen der elastischen Grenzflächen im Hauptspannungsraum inklusive Sensitivitätsanalysen an. Dabei zeigt sich, dass (i) das Zuschlag-Zement-Verhältnis wenig Einfluss auf die Elastizitätsgrenze hat, (ii) die Elastizitätsgrenze mit zunehmendem Wasser-Zement-Wert (w/z) für $w/z > 0{,}42$ signifikant abnimmt und (iii) die Elastizitätsgrenze mit zunehmendem Hydratationsgrad ansteigt. Nur für ausgehärtete Betone bzw. Betone mit kleinem w/z-Verhältnis erhöht ein Anstieg des Seitendrucks die Elastizitätsgrenzen signifikant, während für junge Betone bzw. Betone mit hohem w/z-Wert

der günstige Effekt des Seitendrucks nur gering ist. Der Vergleich der vom Modell vorhergesagten Elastizitätsgrenze mit den Werten der Druckfestigkeit aus dreiaxialen Druckversuchen zeigt, dass (i) die Bruchfestigkeit mit zunehmendem Seitendruck viel stärker ansteigt als die Elastizitätsgrenze und (ii) dass die unelastischen Reserven mit zunehmenden w/z-Wert ansteigen, als Konsequenz der gesteigerten Fähigkeit zur unelastischen Materialverdichtung infolge der erhöhten Porosität.

Contents

Publication outlook: At the time of finalizing this thesis, it is planned to submit this quite mature paper draft —after incorporation of further improvements— for publication to “Construction and Building Materials”.

Chapter 1

Introduction

In many civil engineering structures, such as slabs, plates, shells, and arch dams, concrete is subjected to biaxial or triaxial compressive loading. In contrast to uniaxial compression, the material behavior under triaxial compression is rather ductile. This goes along with large strains before the material fails [49]. The elastic limit is of particular interest for practical engineers, i.e. the stress up to which the material behaves in a linear elastic fashion. Increasing the load beyond the elastic limit leads to nonlinearities in the stress-strain diagram, resulting from irreversible compaction of the microstructure and related cracking [17, 41]. The elastic limit stress is of significant importance for engineers, as it quantifies the threshold for serviceability limit states (SLS) [14, 15, 25–27], which must not be surpassed under characteristic design loads. Experimental determination of multiaxial elastic limits of concrete, see e.g. [2, 9, 10, 17, 18, 22, 24, 41, 45, 47, 48], is limited, because very large loads are required and corresponding experimental devices are rare. Moreover, cementitious materials (pastes, mortars, and concretes) come in a variety of compositions and their elastic limits increase with the materials' maturity. Conducting multiaxial compression experiments for a large variety of concretes at many different material ages, is desirable but out of reach in the context of this work.

Herein, we compute micromechanics-based predictions of elastic limits of concrete. A validated continuum micromechanics multiscale model is used as the vehicle for research in the present work. This model was originally developed for cement paste [38] and then extended to ordinary concrete [31] and recycled concrete [32] by considering failure in interfacial transition zones (ITZs). It relies on elasto-brittle failure upscaling, i.e. failure of the most unfavorably loaded microscopic hydration products located in the most unfavorable ITZ domain is considered to lead to macroscopic material failure. The resulting predictions regarding uniaxial compressive strength values agree with independent experimental results for various compositions and various ages.

In the present master thesis, the model is evaluated for biaxial and triaxial stress states. Given the rather ductile material behavior described above, it is expected that the model delivers elastic limits rather than strength values. In order to provide insight into this topic, the remainder of the master theses is structured as follows. In Section 2, the micromechanics model (Section 2.1) and the triaxial compression test (Section 2.2) are described as necessary prerequisites for the present study. Section 3 is devoted to predicting the elastic limit with the micromechanics model (Section 3.1) and comparing it with the triaxial compression tests (Section 3.2), followed by the illustration of the elastic limit surface for a benchmark concrete in principal stress space (Section 3.3), as well as presenting sensitivity analysis w.r.t. composition and maturity (Section 3.4) and comparing model-predicted elastic limits to experimental strength values (Section 3.5). Section 4 contains the conclusions drawn from the presented study.

Chapter 2

Fundamentals

2.1 Micromechanics of ITZ failure in concrete

The investigation of elastic limits of concrete subjected to multiaxial compressive loading is based on a recently developed continuum micromechanics model of concrete [31]. The material is considered as a macro-homogeneous but micro-heterogeneous body occupying a representative volume element (RVE) with characteristic length ℓ following the scale separation rule [50] reading as

$$d \ll \ell \ll D, \tag{2.1}$$

where d stands for the characteristic size of the inhomogeneities in the RVE, and D represents the characteristic size of either the structure consisting of the RVE or the wavelength of the loading. The required ratios between ℓ and d as well as D and ℓ range from 2 to 3 [13] and from 5 to 50 [28], respectively. Generally, the microstructures of cementitious materials cannot be described in full detail. Therefore, quasi-homogeneous material subdomains are identified (further referred to as "material phases") at different observation scales leading to a hierarchically organized multiscale representation [31, 38, 40]. Each RVE has to satisfy the scale separation rule (2.1) whereby the structural size D, for RVEs resolving inhomogeneities from a larger scale, is equal to the size of these inhomogeneities [19]. "Homogenized" mechanical properties of concrete can be estimated from stepwise "upscaling" accounting for characteristic ellipsoidal phase shapes, (mutual) phase interaction, phase volume fractions, and mechanical phase constants.

Hierarchical organization, phase shape, and interaction are discussed first. To represent ordinary Portland cement-based concrete, we use a hierarchical scheme consisting of three RVEs [38, 40]: concrete, cement paste, and hydrate foam, see Fig. 2.1. The centimeter-sized RVE of concrete [Fig. 2.1(a)] consists of spherical aggregate inclusions (sand grains and gravel, index = agg) embedded inside a cement paste matrix. Cement paste is resolved at the next smaller RVE with a dimension smaller than one millimeter, see Fig. 2.1(b). It contains spherical clinker grains (index = $clin$) embedded in a hydrate foam matrix. At the smallest scale, the 20 micrometer-large hydrate foam [Fig. 2.1(c)] consists of spherical capillary pores (index = $pore$) and needle-shaped hydrates (index = hyd), uniformly orientated in all space directions. As regards the phase interactions, we use the Mori-Tanaka scheme [5, 36] for both matrix-inclusion-type composites (concrete and cement paste) and the self-consistent scheme [20, 21, 33] for the polycrystalline hydrate foam.

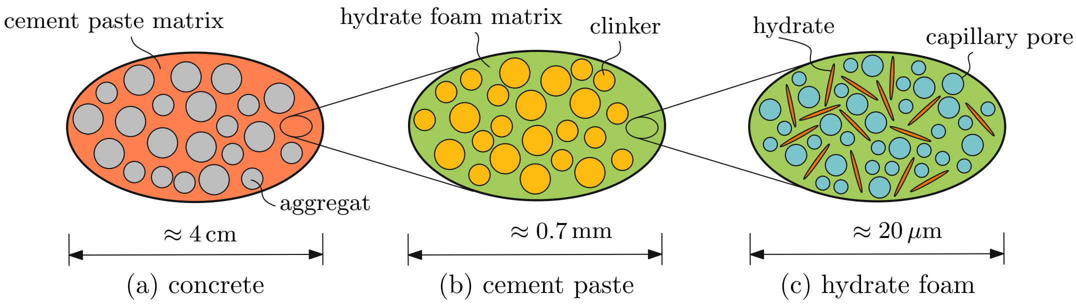

Fig. 2.1: Multiscale micromechanics representation of concrete (material organogram) with its three RVEs and their phases according to Pichler et al. [38, 40]; the 2D sketches show qualitative properties of 3D representative volume elements

Phase volume fractions at the concrete scale [see Fig. 2.1(a)], of aggregates f_{agg}^{con} and of the cement paste f_{cp}^{con}, are determined from the mix-dependent initial aggregate-to-cement mass ratio (a/c), the initial water-to-cement mass ratio (w/c), and the mass densities ρ_i listed in Table 2.1, according to [6]

$$f_{agg}^{con} = \frac{\frac{a/c}{\rho_{agg}}}{\frac{1}{\rho_{clin}} + \frac{w/c}{\rho_{H_2O}} + \frac{a/c}{\rho_{agg}}}\,, \qquad f_{cp}^{con} = 1 - f_{agg}^{con}\,. \tag{2.2}$$

At the scale of cement paste [see Fig. 2.1(b)], the Powers hydration model [38, 42] provides mix-dependent and maturity-dependent phase volume fractions of unreacted clinker, f_{clin}^{cp}, and of the hydrate foam matrix, f_{hf}^{cp}, reading as

$$f_{clin}^{cp} = \frac{20\,(1-\alpha)}{20 + 63\,w/c} \geq 0\,, \qquad f_{hf}^{cp} = 1 - f_{clin}^{cp}\,, \tag{2.3}$$

with the hydration degree α quantifying the material's maturity. It is defined as the ratio of the volume (or mass) of already hydrated clinker, over the initial clinker volume (or mass). At the scale of the hydrate foam [see Fig. 2.1(c)], the Powers hydration model provides the volume fractions of capillary pores, f_{pore}^{hf}, and of hydrates, f_{hyd}^{hf}, as [38]

$$f_{pore}^{hf} = \frac{63\,(w/c - 0.367\,\alpha)}{20\,\alpha + 63\,w/c} \geq 0\,, \qquad f_{hyd}^{hf} = 1 - f_{pore}^{hf}\,. \tag{2.4}$$

Notably, hydration is considered to stop once the hydration degree reaches the maximum value attainable [38]

$$\alpha_{max} = \min\left\{\frac{w/c}{0.42};1\right\}\,. \tag{2.5}$$

The elastic phase constants in terms of bulk moduli k_i and shear moduli μ_i of the phases hydrates ($i\!=\!hyd$), pores ($i\!=\!pore$), clinker ($i\!=\!clin$), and aggregates ($i\!=\!agg$), are taken from the literature, see Table 2.1. Corresponding phase elasticity tensors $\mathbb{C}_i$ read as

$$\mathbb{C}_i = 3\,k_i\,\mathbb{I}^{vol} + 2\,\mu_i\,\mathbb{I}^{dev}\,,\;\; i = \{hyd,\, pore,\, clin,\, agg\}\,, \tag{2.6}$$

where $\mathbb{I}^{vol}$ is the volumetric part of the symmetric fourth-order identity tensor $\mathbb{I}$, and $\mathbb{I}^{dev}$ the deviatoric part. $\mathbb{I}$ is defined as $I_{ijkl} = 1/2(\delta_{ik}\delta_{jl} + \delta_{il}\delta_{jk})$, $\mathbb{I}^{vol}$ as $\mathbb{I}^{vol} = 1/3(\mathbf{1}\otimes\mathbf{1})$, and $\mathbb{I}^{dev}$ as $\mathbb{I}^{dev} = \mathbb{I} - \mathbb{I}^{vol}$, where $\mathbf{1}$ denotes the second-order identity tensor with components equal to the Kronecker delta δ_{ij}, namely $\delta_{ij} = 1$ for $i\!=\!j$, and 0 otherwise.

Tab. 2.1: Phase densities and elastic phase constants

Phase	Mass density [kg/m^3]	Source	Bulk modulus [GPa]	Shear modulus [GPa]	Source
Hydrate	$\rho_{hyd} = 2073$	[11]	$k_{hyd} = 18.70$	$\mu_{hyd} = 11.80$	[7]
Pore	$\rho_{H_2O} = 1000$*		$k_{pore} = 0.00$	$\mu_{pore} = 0.00$	[7]
Clinker	$\rho_{clin} = 3150$	[38]	$k_{clin} = 116.60$	$\mu_{clin} = 53.80$	[1]
Aggregate	$\rho_{agg} = 2650$	[31]	$k_{agg} = 35.35$	$\mu_{agg} = 29.91$	[46]

* Eq. (2.2) is calculated with the mass density of the water in the pores.

As for micromechanics-based predictions of hydrate failure in concrete RVEs, macroscopic stresses $\mathbf{\Sigma}$ are concentrated ("downscaled") into individual hydrates based on the micromechanics representation (hierarchical organization, phase shapes and phase interaction), the phase volume fractions, as well as the elastic phase constants. Therefore, homogeneous macrostresses are first downscaled to spatial averages of cement paste stresses $\boldsymbol{\sigma}_{cp}$ in interfacial transition zones (ITZs) located inside the cement paste matrix in the immediate vicinity of an aggregate, as [31]

$$\boldsymbol{\sigma}_{cp}(\psi,\omega;\mathbf{\Sigma}) = \mathbb{B}_{cp}^{agg}(\psi,\omega) : \mathbb{B}_{agg}^{con} : \mathbf{\Sigma}\,, \tag{2.7}$$

where $\mathbb{B}_{agg}^{con}$ denotes the concrete-to-aggregate stress concentration tensors, $\mathbb{B}_{cp}^{agg}$ denotes the aggregate-to-cement stress concentration tensor accounting for perfect bond between aggregates and cement paste, and (ψ,ω) denote the position angles (zenith and azimuth) on the aggregate-to-cement paste interface $\mathcal{I}_{agg}^{cp}$, see Fig. 2.2(a). Analytical expressions for both stress concentration tensors are given in Appendix A. Position-dependent cement paste stresses $\boldsymbol{\sigma}_{cp}$, are further downscaled to second-order moments of volumetric and deviatoric hydrate stresses as [12, 31]

$$\overline{\overline{\sigma}}_{hyd;\vartheta,\varphi}^{vol}(\psi,\omega;\vartheta,\varphi;\mathbf{\Sigma}) = \sqrt{\lim_{f_{hyd;\vartheta,\varphi}^{cp}\to 0}\left(\frac{3\,k_{hyd}^2}{f_{hyd;\vartheta,\varphi}^{cp}}\,\boldsymbol{\sigma}_{cp}(\psi,\omega;\mathbf{\Sigma}) : \mathbb{C}_{cp}^{-1} : \frac{\partial\mathbb{C}_{cp}}{\partial k_{hyd;\vartheta,\varphi}} : \mathbb{C}_{cp}^{-1} : \boldsymbol{\sigma}_{cp}(\psi,\omega;\mathbf{\Sigma})\right)}\,, \tag{2.8}$$

$$\overline{\overline{\sigma}}_{hyd;\vartheta,\varphi}^{dev}(\psi,\omega;\vartheta,\varphi;\mathbf{\Sigma}) = \sqrt{\lim_{f_{hyd;\vartheta,\varphi}^{cp}\to 0}\left(\frac{2\,\mu_{hyd}^2}{f_{hyd;\vartheta,\varphi}^{cp}}\,\boldsymbol{\sigma}_{cp}(\psi,\omega;\mathbf{\Sigma}) : \mathbb{C}_{cp}^{-1} : \frac{\partial\mathbb{C}_{cp}}{\partial \mu_{hyd;\vartheta,\varphi}} : \mathbb{C}_{cp}^{-1} : \boldsymbol{\sigma}_{cp}(\psi,\omega;\mathbf{\Sigma})\right)}\,, \tag{2.9}$$

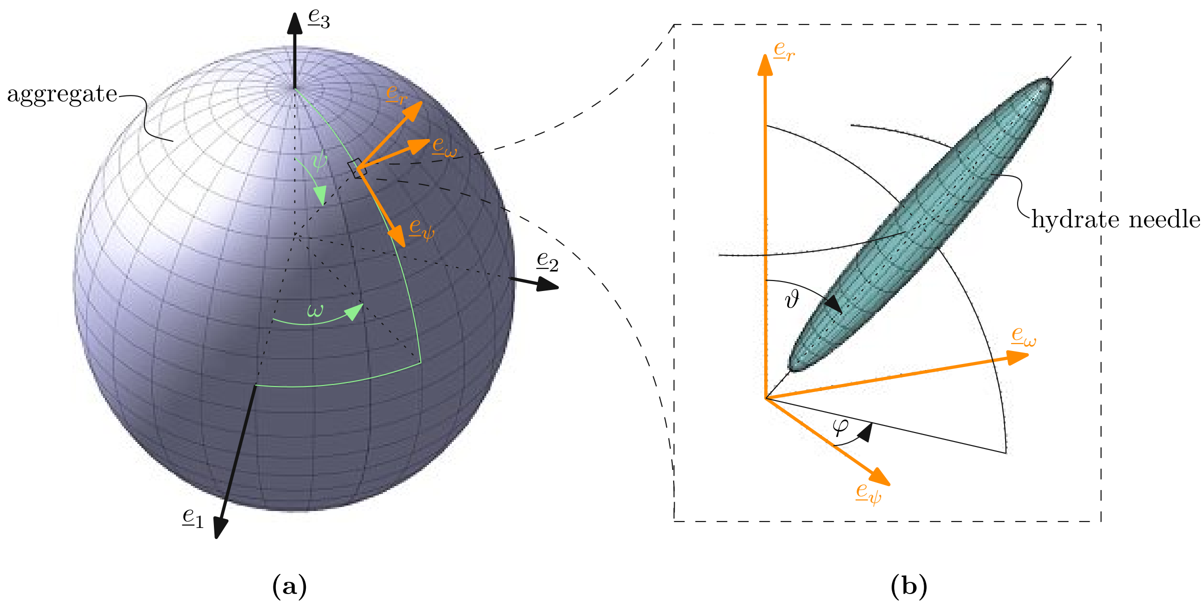

Fig. 2.2: (a) Zenith angles ψ and azimuth angle ω defining the position of the cement paste RVE along the aggregate surface with global Cartesian base $\underline{e}_1$, $\underline{e}_2$, $\underline{e}_3$, and local spherical base $\underline{e}_r$, $\underline{e}_\omega$, $\underline{e}_\psi$; (b) Zenith angle φ and azimuth angle ϑ defining the orientation of the hydrate needle with respect to the spherical base

where (ϑ, φ) denote the hydrate orientation [zenith and azimuth angle, see Fig 2.2(b)], $\mathbb{C}_{cp}$ stands for the homogenized elasticity tensor of cement paste (see Appendix A for analytical formulas regarding stiffness homogenization), and $f^{cp}_{hyd;\vartheta,\varphi} = V_{hyd;\vartheta,\varphi}/V_{cp}$ is the cement paste-related volume fraction of (ϑ, φ)-oriented hydrates. Hydrate failure is quantified according to a Drucker-Prager failure criterion based on second-order moments of stresses (2.8) and (2.9) reading as [31]

$$f_{DP}(\overline{\overline{\boldsymbol{\sigma}}}_{hyd}) = \frac{\overline{\overline{\sigma}}^{dev}_{hyd}}{\sqrt{2}} - k^{DP}_{hyd} + \alpha^{DP}_{hyd} \frac{\overline{\overline{\sigma}}^{vol}_{hyd}}{\sqrt{3}} \leq 0\,. \tag{2.10}$$

The Drucker-Prager constants for the hydrate needle phase, k^{DP}_{hyd} and α^{DP}_{hyd}, are quantified based on the friction angle $\phi = 12°$ and the cohesion $c = 50\,\text{MPa}$ of the Mohr-Coulomb failure criterion, determined from limit state analyzes of nanoindentation tests [11, 44], resulting in [31]

$$k^{DP}_{hyd} = 60.68\,\text{MPa} \quad \text{and} \quad \alpha^{DP}_{hyd} = 0.2580\,. \tag{2.11}$$

To quantify the relevant position $(\psi_{crit}, \omega_{crit})$ of cement paste RVEs along the aggregate-cement paste interface and relevant hydrate orientation $(\vartheta_{crit}, \varphi_{crit})$, the maximum of the failure function is searched for, $f_{DP} \rightarrow \max$. The macroscopic stress state $\boldsymbol{\Sigma}^{lim}$, for which the most heavily loaded hydrates fail, $f_{DP}(\psi_{crit}, \omega_{crit}; \vartheta_{crit}, \varphi_{crit}, \boldsymbol{\Sigma}^{lim}) = 0$, is considered as the elastic limit stress of concrete. The model-predicted limit stress for uniaxial compressive loading has been shown to agree very well with experimentally determined uniaxial compressive strength values of cement pastes, mortars, and concretes at various material maturities, see [31].

2.2 Triaxial compression testing of concrete

Results from several triaxial compression testing campaigns on concretes, taken from the literature, are described. Six triaxial compression test campaigns involving eight concrete compositions with water-to-cement ratios w/c ranging from 0.23 to 0.75 and aggregate-to-cement ratios a/c ranging from 3.18 to 7.62 are described in [17, 18, 22, 24, 41, 45], see Table 2.2. All concretes were tested at ages of two months or more, except for Hampel et al. [18] who performed the tests between 28 and 35 days after production. Uniaxial compressive strength values f_c^{uni} were determined for most compositions and ranged from 28.6 to 73.35 MPa. Triaxial compression tests were either performed in a triaxial compression cell on cylindrical specimens with diameters d ranging from of 54 to 150 mm and heights h ranging from 115 to 300 mm [24, 41, 45], see Fig. 2.3(a), or on cuboidal specimens with side lengths a, b, c ranging from 40 to 150 mm [17, 18, 22], see Fig. 2.3(b). In order to reduce the friction between the loading apparatus and the specimens, Sfer et al. [45] and Geel [17] used Teflon sheets, while Hussein and Marzouk [22] as well as Hampel et al. [18] used brush-type loading plates. Imran and Pantazopoulou [24] as well as Poinard et al. [41] do not report on measures for friction reduction. In order to quantify the displacements, linear variable differential transformers (LVDTs) [17, 18, 22, 24, 41, 45], extensometers [22] and strain gauges [22, 24, 45] were used.

Tab. 2.2: Properties of the concretes tested in the experiments

Source	Mix	w/c [–]	a/c [–]	Geometry [mm]	Age [months]	f_c^{uni} [MPa]	α [–]	Σ_{ini} [MPa]	β_1 [–]	β_2 [–]
[45]	Sf 1	0.57	5.30	cylinder: $d = 150$ $h = 300$	3.5 to 3.8	38.80	0.79	1.5 to 30.0	0.00	0.00
[24]	Im 1	0.40	3.68	cylinder: $d = 54$ $h = 115$	3.5	73.35	0.78	38.4	0.00	0.00
	Im 2	0.55	5.38			47.40	0.85	8.6	0.00	0.00
	Im 3	0.75	7.62			28.62	0.90	21.0	0.00	0.00
[17]	Ge 1	0.50	4.82	cube: $a = b = c = 100$	2 to 2.5	44.00	0.73	3.0 to 50.0	0.00	0.00
[22, 23]	Hu 1	0.47	5.00	cuboid: $a \times b \times c$ $40 \times 150 \times 150$	≥ 2	44.30	0.68	0.0	0.00	0.20 to 1.00
[18]	Ha 1	0.40	4.60	cube: $a = b = c = 100$	0.9 to 1.2	57.70	0.66	0.0	0.15	0.20
[41]	Po 1	0.64	7.02	cylinder: $d = 70$ $h = 140$	3	–	1.00	0.0	1.00	1.00

The specimen were subjected to triaxial compressive stress states $\mathbf{\Sigma}$, defined as:

$$\mathbf{\Sigma} = -\Sigma_1\, \underline{e}_1 \otimes \underline{e}_1 - \Sigma_2\, \underline{e}_2 \otimes \underline{e}_2 - \Sigma_3\, \underline{e}_3 \otimes \underline{e}_3\,, \tag{2.12}$$

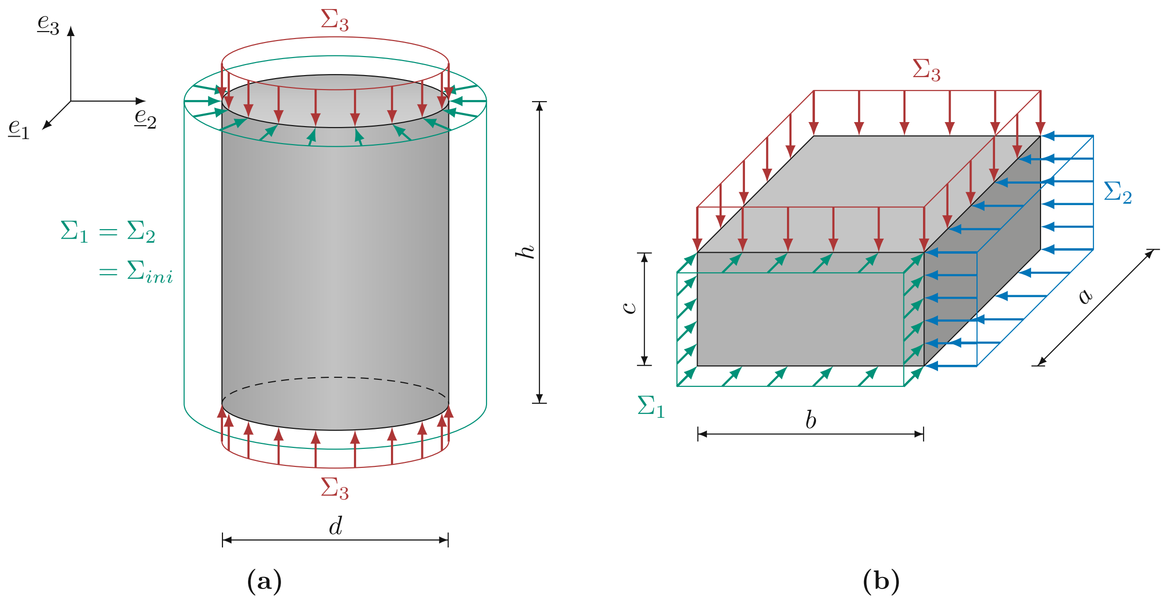

Fig. 2.3: Specimen geometry used for triaxial compression tests: (a) cylinders, (b) cuboids

where $0 \leq \{\Sigma_1, \Sigma_2\} \leq \Sigma_3$ are the principal stresses in the principal stress directions $\underline{e}_1$, $\underline{e}_2$, and $\underline{e}_3$, respectively. The principal stresses were either proportionally increased, or the specimens were first subjected to a hydrostatic stress state $\Sigma_1 = \Sigma_2 = \Sigma_3 = \Sigma_{ini}$, followed by an increase of the stress component Σ_3 while maintaining $\Sigma_1 = \Sigma_2 = \Sigma_{ini}$. The latter type of test is referred to as triaxial test with axial symmetry. Mathematically, the described test protocols can be expressed as

$$\begin{aligned} \Sigma_1(\lambda) &= \Sigma_{ini} + \lambda\,\beta_1 \cdot 1\,\text{MPa}\,, \\ \Sigma_2(\lambda) &= \Sigma_{ini} + \lambda\,\beta_2 \cdot 1\,\text{MPa}\,, \\ \Sigma_3(\lambda) &= \Sigma_{ini} + \lambda \cdot 1\,\text{MPa}\,, \end{aligned} \tag{2.13}$$

where $\lambda \geq 0$ stands for a dimensionless load parameter. β_1 and β_2 are dimensionless stress ratios. For $\Sigma_{ini} = 0$, they read as $\beta_1 = \Sigma_1/\Sigma_3$ and $\beta_2 = \Sigma_2/\Sigma_3$, whereby $0 \leq \beta_1 \leq 1$ and $0 \leq \beta_2 \leq 1$. Triaxial compression tests with axial symmetry, as reported in [17, 24, 45], can be expressed by specifying Eq. (2.13) for $\Sigma_{ini} > 0$ and $\beta_1 = \beta_2 = 0$, see Table 2.2 for details and Fig. 2.4(a) for a graphical representation. Proportionally loaded biaxial and triaxial compression tests, as reported in [18, 22], can be expressed by specifying Eq. (2.13) for $\Sigma_{ini} = 0$, $\beta_1 = 0$ and $\beta_2 > 0$ and $\beta_1 = 0.15$ and $\beta_2 = 0.20$, respectively. Hydrostatic compression tests, as reported in [41], can be expressed by specifying Eq. (2.13) for $\Sigma_{ini} = 0$, $\beta_1 = \beta_2 = 1$, see Fig. 2.4(b).

Material behavior of concrete observed in the six test campaigns is discussed based on stress-strain diagrams provided by the experimenters, see Figs. 2.5 and 2.6. All stress-strain curves start with a virtually linear branch. With increasing compressive loading, concrete softens, leading to progressively increasing non-linearities.

- Regarding triaxial compression tests with axial symmetry [17, 24, 45], the strength of concrete ($\max \Sigma_3$) increases significantly with increasing lateral pressure $\Sigma_1 = \Sigma_2$, see

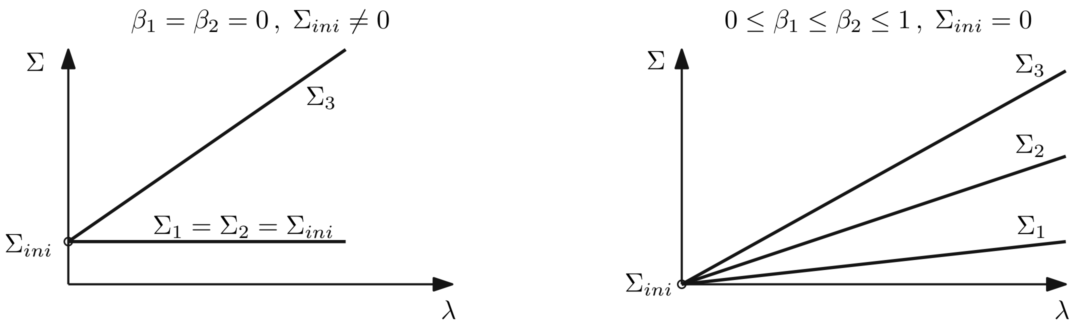

(a) Triaxial compression tests with axial symmetry **(b)** Proportionally loaded compression test

Fig. 2.4: Load histories applied in the analyzed experiments

Fig. 2.5. As for small lateral pressure, $\Sigma_1 = \Sigma_2 < 20$ MPa, a stress peak is clearly identifiable, followed by a rather ductile failure associated with slowly decreasing axial stresses while axial strains E_3 are further increasing. As for larger lateral pressure $\Sigma_1 = \Sigma_2 > 20$ MPa, axial stresses continuously increase with increasing strain. The stress peak is not well defined and the strength degradation afterwords is rather small and in some cases almost not observed [24, 45].

- Regarding compression test with proportional loading, the stress strain curves are qualitatively similar to each other, see Fig. 2.6. The strength Σ_3 obtained from biaxial compression tests is larger for $\beta_2 = 0.5$, compared to $\beta_2 \in \{0.2, 1\}$, see Fig. 2.6(a). Poinard et al. [41] is the only one who used cycles of loading and unloading, see Fig. 2.6(c).

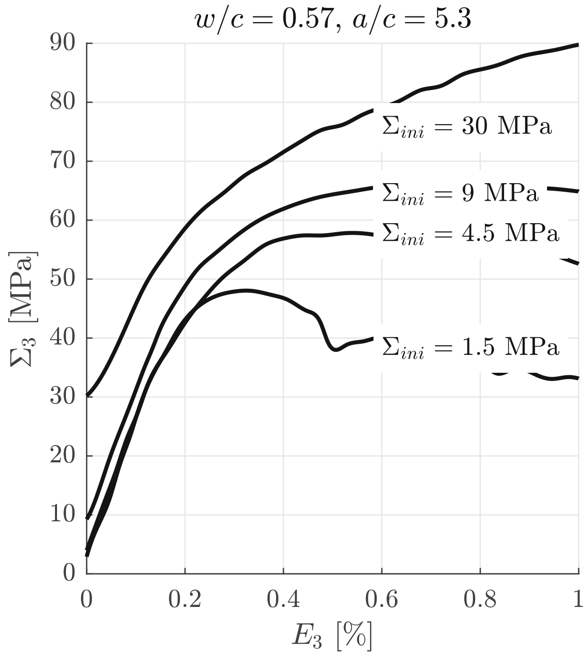

(a) Experimental data from Sfer et al. [45]

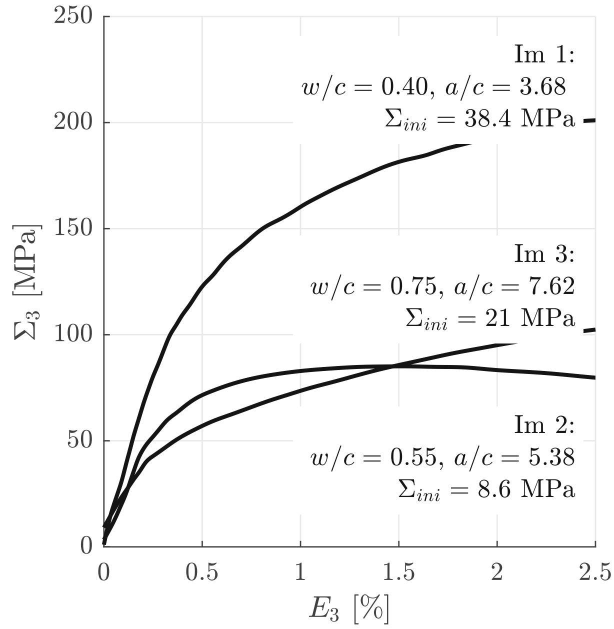

(b) Experimental data from Imran and Pantazopoulou [24]

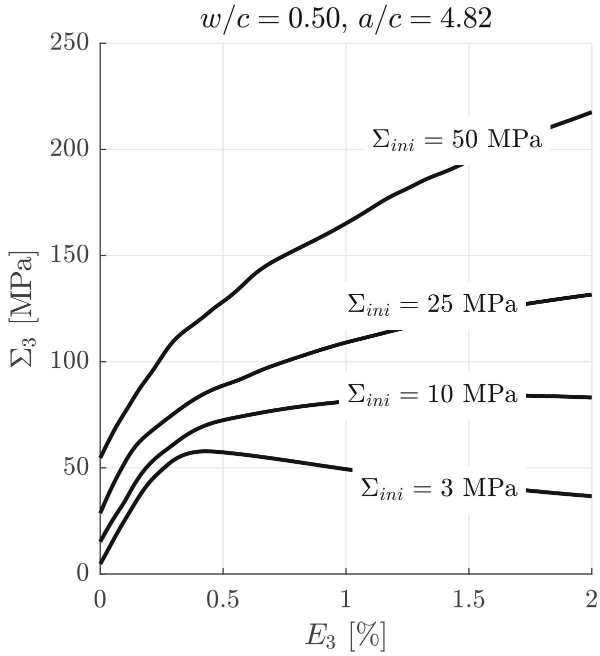

(c) Experimental data from Geel [17]

Fig. 2.5: Stress-strain curves determined in triaxial compression tests with axial symmetry; the load paths are characterized by $\Sigma_{ini} > 0$ and $\beta_1 = \beta_2 = 0$ in Eq. (2.13)

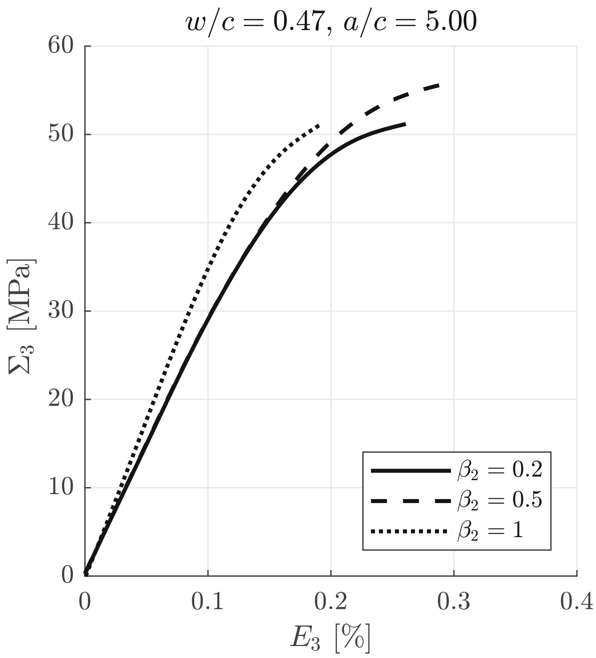

(a) Experimental data from Hussein [23]

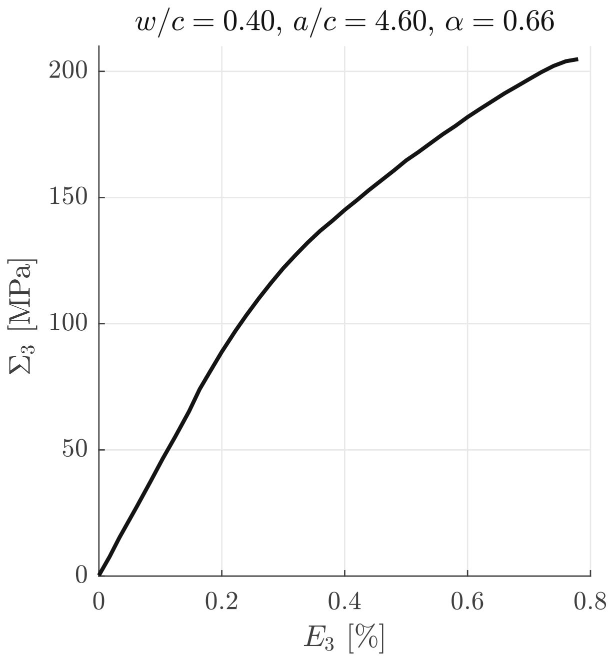

(b) Experimental data from Hampel et al. [18]

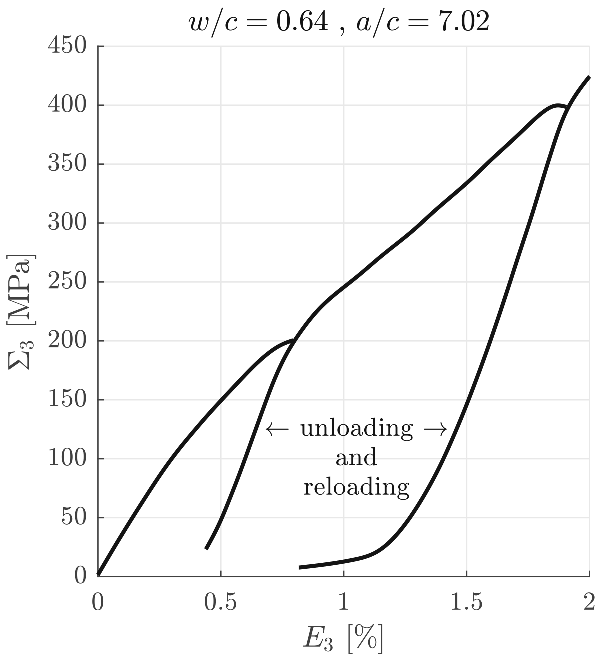

(c) Experimental data from Poinard et al. [41]

Fig. 2.6: Stress-strain curves determined in proportionally loaded compression tests; the load paths in (a) are characterized by specifying Eq. (2.13) for $\Sigma_{ini} = 0$, $\beta_1 = 0$, and $\beta_2 > 0$ (biaxial compression), in (b) for $\Sigma_{ini} = 0$, $\beta_1 = 0.15$, and $\beta_2 = 0.2$ (triaxial compression), and in (c) for $\Sigma_{ini} = 0$, $\beta_1 = \beta_2 = 1$ (hydrostatic compression)

Chapter 3

Multiscale analysis of hydrate failure in ITZs in multiaxial compression tests on concrete

3.1 Model evaluation and algorithmic treatment of triaxial compression tests

To evaluate the elastic limits for the six tested concretes [17, 18, 22, 24, 41, 45] described in Section 2.2 and summarized in Table 2.2, the test-specific concrete composition (w/c and a/c) is inserted into the Powers' expressions of the phase volume fractions Eq. (2.2) to (2.4). Test-specific hydration degrees α are not reported. As a remedy, they are back-identified from the measured *uniaxial* compressive strength values, given in Table 2.2. To this end, the micromechanics model described in Section 2.1, is evaluated for varying hydration degrees α until the difference between model-predicted and experimentally determined *uniaxial* compressive strength values vanishes, see Table 2.2 for the resulting hydration degrees. Hydration degrees are generally close to one, given the mature age of the tested concretes. Notably, as Poinard et al. [41] did not measure the uniaxial compressive strength, $\alpha = 1$ is assumed for this composition.

Elastic limits for concretes subjected to multiaxial macrostresses are obtained from Drucker-Prager failure of the most unfavorably loaded hydrate-gel needle phase situated inside the most unfavorably loaded ITZ domain. The algorithmic treatment to identify the critical hydrate and the critical ITZ domain depends on the loading path, as described next:

- As for triaxial compression tests with axial symmetry performed by Imran and Pantazopoulou [24], Sfer et al. [45], and Geel [17], we check that the initial macrostress state $\mathbf{\Sigma}(\Sigma_{ini}, \beta_1 = \beta_2 = 0, \lambda = 0)$ —according to macrostress definition Eq. (2.13) and test-specific loading variable Σ_{ini} from Table 2.2— does not already lead to failure. Therefore, macrostresses are downscaled to second-order moments of hydrate stresses according to Eqs. (2.8) and (2.9), resulting in position-dependent [angles ψ and ω according to Fig. 2.2(a)] and orientation-dependent [angles ϑ and φ according to Fig. 2.2(b)] hydrate stresses. The Drucker-Prager failure criterion Eq. (2.10) is evaluated for all positions along the aggregate surface and all hydrate orientations $f_{DP}[\psi, \omega; \vartheta, \varphi, \mathbf{\Sigma}(\Sigma_{ini}, \lambda = 0)]$. Only if all hydrates are still intact ($f_{DP} < 0$), the macrostress is increased by increasing the load factor λ. This new stress state $\mathbf{\Sigma}(\Sigma_{ini}, \lambda > 0)$ is again downscaled, and hydrate failure is again assessed by means of the Drucker-Prager failure criterion Eq. (2.10). Only if all hydrates are intact, the load is further increased. This procedure is repeated until any subdomain of the hydrates fail, indicated by $f_{DP}[\psi_{crit}, \omega_{crit}; \vartheta_{crit}, \varphi_{crit}, \mathbf{\Sigma}^{lim}(\Sigma_{ini}, \beta_1 = \beta_2 = 0, \lambda_{crit})] = 0$, where $\mathbf{\Sigma}^{lim}$ is the elastic limit, λ_{crit} is the corresponding load factor, angles ψ_{crit}, ω_{crit} indicate the relevant location at the aggregate surface and ϑ_{crit}, φ_{crit} indicate the relevant hydrate orientation. The relevant position (ψ_{crit} and ω_{crit}) and the relevant orientation angles (ϑ_{crit} and φ_{crit}) indicating the most unfavorably loaded ITZ domain and hydrate, respectively, may change with increasing load factor λ.

- As for *proportionally* loaded compression tests performed by Hussein and Marzouk [22], Poinard et al. [41], and Hampel et al. [18], the position and the orientation of the most unfavorably loaded ITZ domain and hydrate do not change with respect to the load factor λ. This way, the evaluation of the elastic limit is simplified and stress downscaling can be limited to only one value of the load factor λ. Macrostresses $\mathbf{\Sigma}(\Sigma_{ini} = 0, \beta_1, \beta_2, \lambda)$ are again downscaled to hydrate stresses. Based on the Drucker-Prager failure criterion, the most unfavorably loaded ITZ domain and hydrate needle are searched for: $f_{DP} \rightarrow \max$, yielding the relevant angles $\Rightarrow \psi_{crit}, \omega_{crit}; \vartheta_{crit}, \varphi_{crit}$. The relevant load factor λ_{crit} is then obtained from solving $f_{DP}[\psi_{crit}, \omega_{crit}; \vartheta_{crit}, \varphi_{crit}, \mathbf{\Sigma}^{lim}(\Sigma_{ini} = 0, \beta_1, \beta_2, \lambda_{crit})] = 0$, and the corresponding macrostress state $\mathbf{\Sigma}^{lim} = \mathbf{\Sigma}(\Sigma_{ini} = 0, \beta_1, \beta_2, \lambda_{crit})$ is the sought elastic limit $\mathbf{\Sigma}^{lim}$.

3.2 Comparison of model-predicted elastic limits to experimental stress-strain curves

Model-predicted elastic limits agree, for all ten studied concrete compositions, well with the initiation of major nonlinearities in the experimentally determined stress-strain curves, see Fig. 3.1 and 3.2. This underlines that onset of ITZ-driven failure corresponds to the end of the virtually elastic region, and that the model is also relevant for *multiaxially* compressed concretes. In this context, we note that upscaling of microscopic ITZ failure for uniaxially compressed concretes yields very good predictions for the macroscopic strength values [31]. As for multiaxially compressed concretes, in turn, upscaling of ITZ failure yields macroscopic elastic limits which are lower than the strength values. In contrast to uniaxial compression tests, loading above the limit stresses $\mathbf{\Sigma}^{lim}$ is possible, but leads to inelastic volume compaction accompanied by large strains [17].

The elastic limits of concrete increase with increasing lateral pressure, see the stress strain curves of Sfer et al. [45] and Geel [17] in Fig. 3.1(a, c), but the difference between the largest lateral pressure and the smallest lateral pressure is rather small. This experimental observation is very well captured by the model. Elastic limits for the test of Sfer et al. [45] with $\Sigma_{ini} = 30\,\mathrm{MPa}$ amount to $\Sigma_3^{lim} = 48.2\,\mathrm{MPa}$, while for the tests with $\Sigma_{ini} = 1.5\,\mathrm{MPa}$, elastic limits amount to $\Sigma_3^{lim} = 39.7\,\mathrm{MPa}$, and are thus only by 17.6 % smaller. By analogy, the elastic limit for the test of Geel [17] with the smallest lateral pressure $\Sigma_{ini} = 3\,\mathrm{MPa}$ ($\Sigma_3^{lim} = 45.5\,\mathrm{MPa}$) is only by 21.8 % smaller than the elastic limit for the tests with the largest lateral pressure $\Sigma_{ini} = 50\,\mathrm{MPa}$ ($\Sigma_3^{lim} = 58.2\,\mathrm{MPa}$). The corresponding strength values, i.e. the experimentally measured peak stresses (if observable), significantly increase with increasing lateral pressure. The discussion on the difference between strength values and elastic limits is continued in Section 3.5.

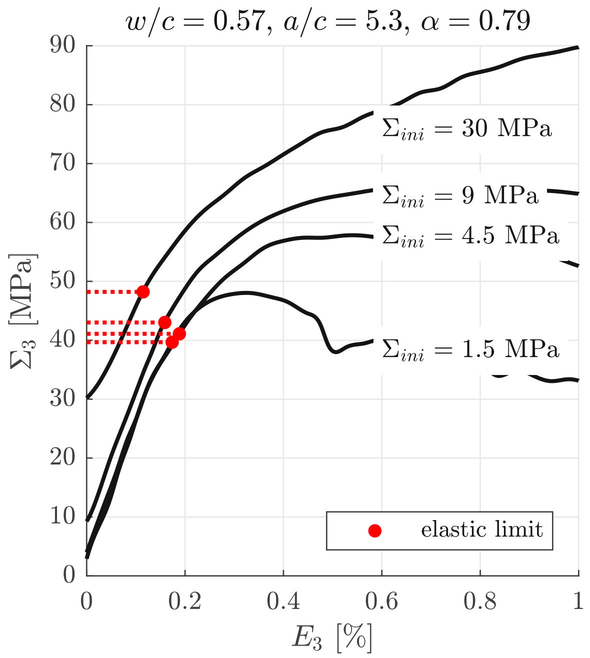

(a) Experimental data from Sfer et al. [45]

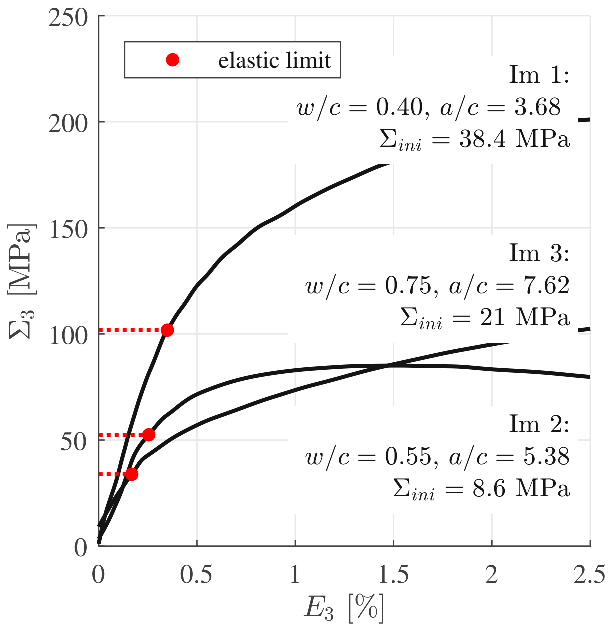

(b) Experimental data from Imran and Pantazopoulou [24]

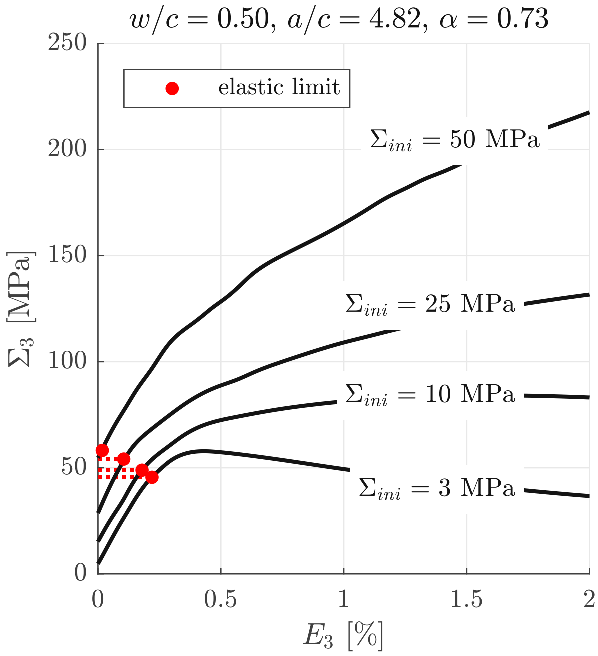

(c) Experimental data from Geel [17]

Fig. 3.1: Model validation: Comparison of predicted elastic limits with experimental stress-strain curves from Fig. 2.5 for triaxial compression tests with axial symmetry

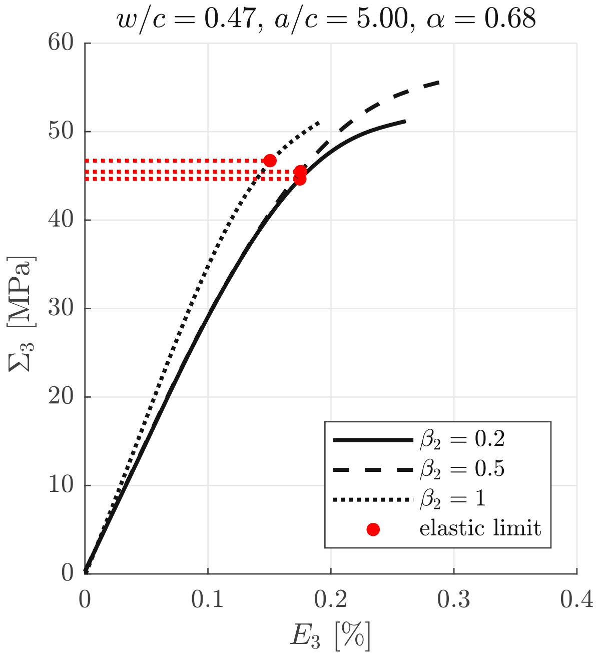

(a) Experimental data from Hussein [23]

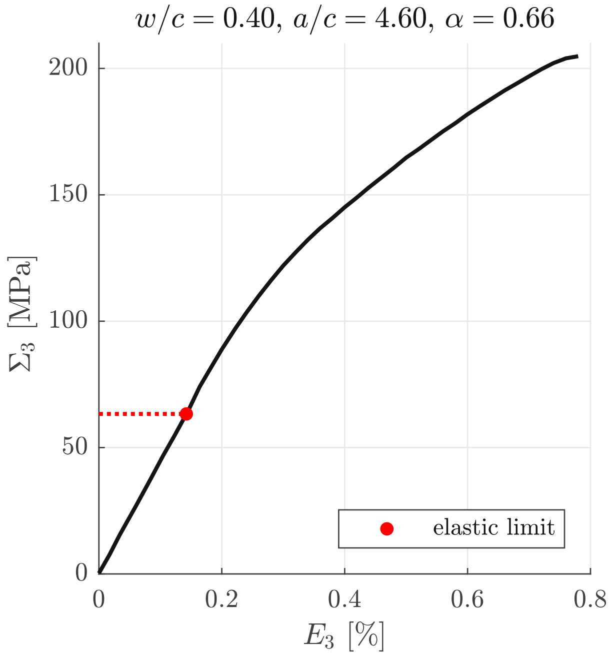

(b) Experimental data from Hampel et al. [18]

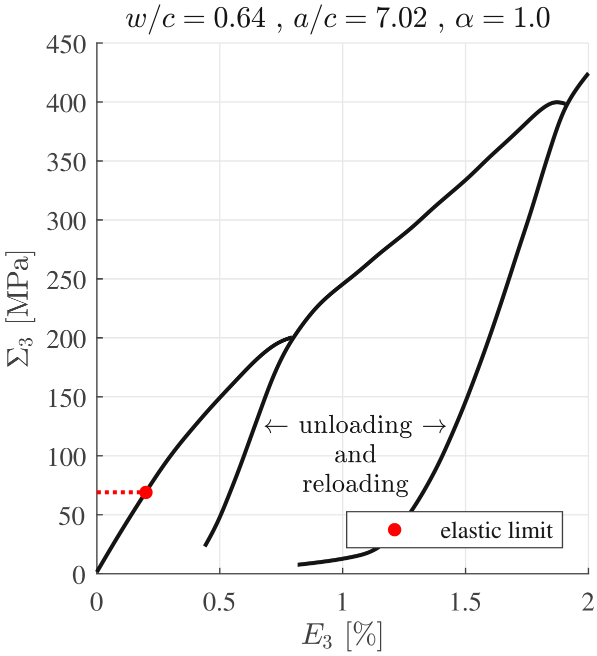

(c) Experimental data from Poinard et al. [41]

Fig. 3.2: Model validation: Comparison of predicted elastic limits with experimental stress-strain curves from Fig. 2.6 for (a) biaxial, (b) triaxial, and (c) hydrostatic proportional compression tests

3.3 Model-predicted elastic limit surfaces in principal stress space

The promising model performance regarding elastic limits under multiaxial compression motivates us to study model-predictions for general compressive loading scenarios. Therefore, we focus on a fully hydrated and proportionally loaded benchmark concrete (hydration degree $\alpha = 1$ and $\Sigma_{ini} = 0$) with w/c ratio amounting to 0.5 and a/c ratio amounting to 5.0. The predicted elastic limits under uniaxial, symmetric biaxial, and hydrostatic compression, Σ_{uni}^{lim}, Σ_{bi}^{lim}, and Σ_{hyd}^{lim}, amount to 71.0, 78.8, and 148.3 MPa, respectively. Evaluating the elastic limit for all possible combinations of Σ_1, Σ_2, and Σ_3 yields an elastic limit surface in principal stress space (see Fig. 3.3). Its tip is located at the hydrostatic axis defined as $\Sigma_1 = \Sigma_2 = \Sigma_3$. Stress states inside the convex elastic limit surface refer to intact ITZs and thus elastic material behavior. Stress states at the surface refer to elastic limits.

We discuss three types of plane sections through the elastic limit surface in the principal stress space, resulting in three elastic limit envelopes. In this context Haigh-Westergaard coordinates are introduced: the hydrostatic coordinate ξ, the deviatoric coordinate r, and the Lode angle θ, see Appendix B. Biaxial elastic limit envelopes are obtained by cutting the elastic limit surface with the Σ_2, Σ_3-plane, see Fig. 3.4(a). The elastic limit Σ_3^{lim} increases monotonously with increasing stress component Σ_2. Cutting the elastic limit surface normal to the hydrostatic axis yields elastic limit envelopes in the deviatoric plane. Two such envelopes are illustrated in Fig. 3.4(b): one contains the hydrostatic symmetric biaxial compression $\xi = \xi(\Sigma_{bi}^{lim})$, the other is located at $\xi = 2/3\,\xi_{max}$, with $\xi_{max} = \Sigma_{hyd}^{lim}/\sqrt{3}$ as the hydrostatic coordinate at the tip of the limit surface. The former deviatoric elastic limit envelope exhibits a hexagonal shape resembling a Mohr-Coulomb limit surface, the latter a triangle-shaped. The maximum sustainable deviatoric stress (the maximum of the deviatoric coordinate r) coincides with the symmetric biaxial compression stress state ($\Sigma_2 = \Sigma_3 = \Sigma_{bi}^{lim}$, $\Sigma_3 = 0$). This is also observed in the envelopes resulting from plane sections through the elastic limit surface, with cutting planes containing the hydrostatic axis, see Fig. 3.4(c) for envelopes with Lode angles $\theta =\in \{0°, 30°, 60°\}$. The uniaxial compression stress Σ_{uni}^{lim} refers to Lode angle $\theta = 60°$, symmetric biaxial compression to Lode angle $\theta = 0°$.

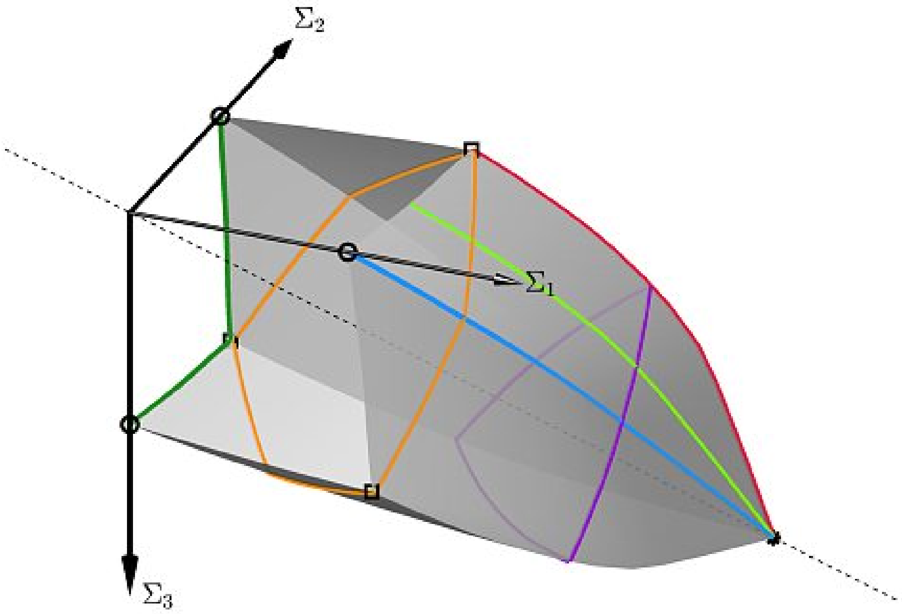

Fig. 3.3: 3D view of the elastic limit surface in principal stress space of a fully hydrated benchmark concrete ($w/c = 0.5$, $a/c = 5$, and $\alpha = 1$); the colored lines refer to the elastic limit envelopes in Fig. 3.4, the dashed line is the hydrostatic axis and the circle, square, and star points refer to the uniaxial, symmetric biaxial, and the hydrostatic elastic limit, respectively

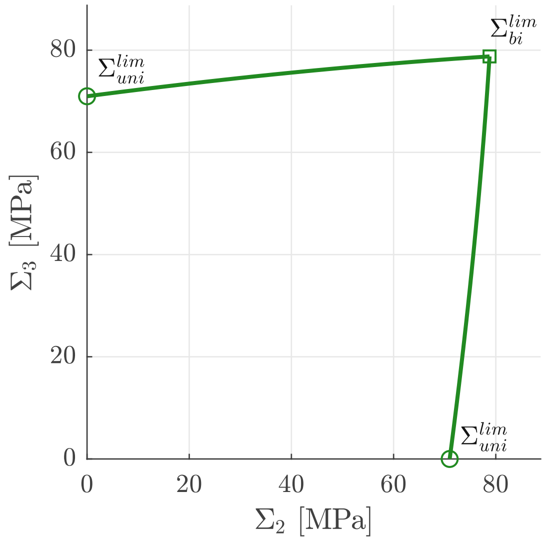

(a) Cross section through the biaxial plane

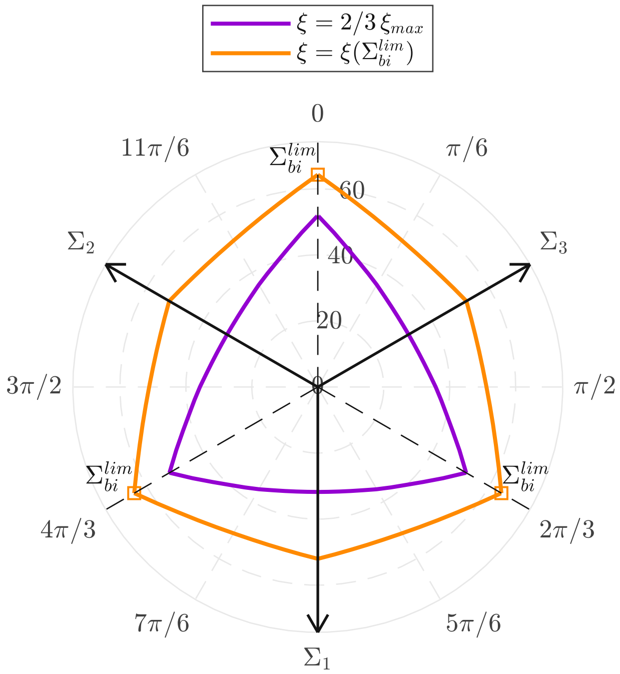

(b) Cross section through the deviatoric plane

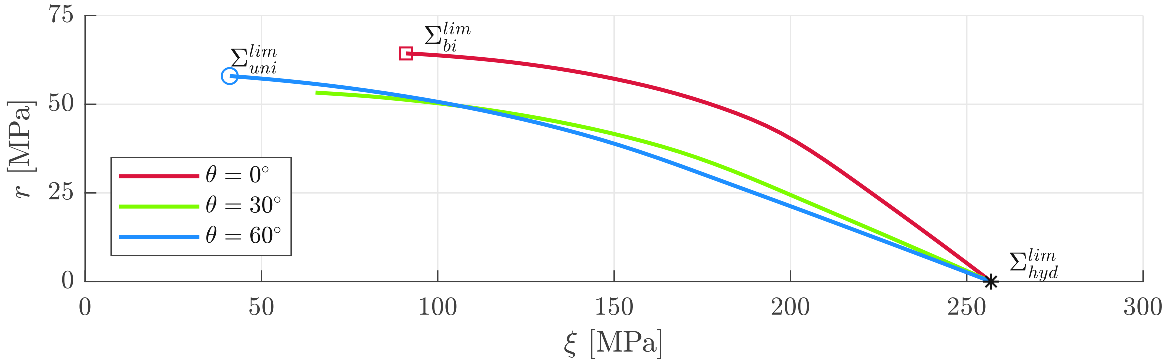

(c) Cross sections along the hydrostatic axis

Fig. 3.4: Elastic limit envelopes of a fully hydrated benchmark concrete ($w/c = 0.5$, $a/c = 5$ and $\alpha = 1$) in three different sections through the elastic limit surface; note that positive values are compression; the individual elastic limit envelopes can be retrieved in the 3D elastic limit surface Fig. 3.3

3.4 Sensitivity analysis w.r.t. composition and maturity

The promising model performance also provides the motivation for sensitivity analysis, i.e. the model is evaluated for different concretes and different maturities. The influences of the aggregate-to-cement ratio $a/c \in [3, 8]$, the water-to-cement ratio $w/c \in [0.2, 0.8]$, and the hydration degree $\alpha \in [0, \alpha_{max}]$, with α_{max} according to Eq. (2.5), on the predicted elastic limits of the benchmark concrete ($w/c = 0.5$, $a/c = 5$, $\alpha = \alpha_{max}$) is investigated. Therefore, we evaluate the model for four loading scenarios: uniaxial loading with $\beta_1 = 0.0$ and $\beta_2 = 0.0$, symmetric biaxial loading with $\beta_1 = 0.0$ and $\beta_2 = 1.0$, a characteristic triaxial loading with $\beta_1 = 0.3$ and $\beta_2 = 0.3$, and hydrostatic loading with $\beta_1 = 1.0$ and $\beta_2 = 1.0$; all of which refer to proportional loading with $\Sigma_{ini} = 0$. Model-predicted elastic limits increase (i) moderately with increasing a/c ratio, (ii) significantly with increasing hydration degree α, and (iii) significantly with decreasing w/c ratio, at least in the regime $w/c > 0.42$, see Fig. 3.5. The kink in Fig. 3.5(b) at $w/c = 0.42$ results from the effect that there is not enough water for complete hydration ($\alpha_{max} < 1$) in concretes with $w/c < 0.42$, but full hydration of the cement is possible for concretes with $w/c \geq 0.42$, see Eq. (2.5). As for uniaxial, symmetric biaxial, and characteristic triaxial loading, the decrease of the elastic limit with increasing w/c-ratio is small up to $w/c < 0.42$, but significant thereafter. As for hydrostatic compression, the elastic limit is virtually constant at $\Sigma_3^{lim} \approx 400\,\text{MPa}$ for $w/c \in [0.2, 0.42]$, which is roughly three times larger than the elastic limit related to the other three loading scenarios, and the elastic limit decreases sharply with increasing w/c ratios for $w/c > 0.42$, see the blue graph in Fig. 3.5(b). At $w/c = 0.8$, it amounts to $\Sigma_3^{lim} \approx 35\,\text{MPa}$, and is very close to the elastic limits related to the other three loading scenarios. This shows that the beneficial confinement pressure effect on the elastic limit is particularly large for concretes with small w/c ratios.

Given the moderate influence of the aggregate-to-cement ratio a/c on the elastic limit of concrete, we study the sensitivity of the water-to-cement ratio w/c and hydration degree α, but keep the aggregate-to-cement ratio constant at $a/c = 5$. In more detail, we consider two water-to-cement ratios $w/c = \{0.3, 0.5\}$, and four different hydration degrees $\alpha = \{0.25, 0.5, 0.75, 1.0\} \times \alpha_{max}$ with α_{max} amounting to 0.71 and 1, respectively, see also Eq. (2.5). For these $2 \times 4 = 8$ concretes, the elastic limit envelopes introduced in Section 3.3 are analyzed. Again, the elastic limit increases with increasing hydration degree and decreasing water-to-cement ratio, see Fig. 3.6, Fig. 3.7, and Fig. 3.8. As for reference, Σ_{uni}^{lim}, Σ_{bi}^{lim} and Σ_{hyd}^{lim} are marked with circles, squares, and stars, respectively. The symmetric biaxial elastic limit is always slightly larger than the respective uniaxial elastic limit, see Fig. 3.6, indicating a small benefit due to the additional lateral pressure in $\underline{e}_2$ direction. The symmetric biaxial elastic limit Σ_{bi}^{lim} increases, by roughly 150 % for all hydration degrees $\alpha = \{0.25, 0.5, 0.75, 1.0\} \times \alpha_{max}$ when the w/c-ratio decreases from 0.5 to 0.3. Comparing the symmetric biaxial elastic limit at hydration degree $\alpha = 0.5\,\alpha_{max}$ to $\alpha = 1.0\,\alpha_{max}$, the increase amounts to 353 % and 371 % for $w/c = 0.3$ and $w/c = 0.5$, respectively. The deviatoric elastic limit envelope changes its shape: it is close to a equilateral triangle for young concretes, but resembles a hexagonal polygon, similar to the Mohr-Coulomb limit surface, for mature concretes, see Fig. 3.7. The cross sections along the hydrostatic axis reveal a steady grow of the elastic limit surface with increasing hydration degree, see Fig. 3.8. The deviatoric coordinate r is monotonously decreasing with increasing hydrostatic stress ξ for most concretes this decrease is particularly sharp for young ones. Only for fully hydrated concrete with $w/c = 0.3$, a slight increase for increasing ξ is obtained. This goes along with an elastic limit envelope which extends long along the hydrostatic axis shape for fully hydrated concretes with low w/c-ratio.

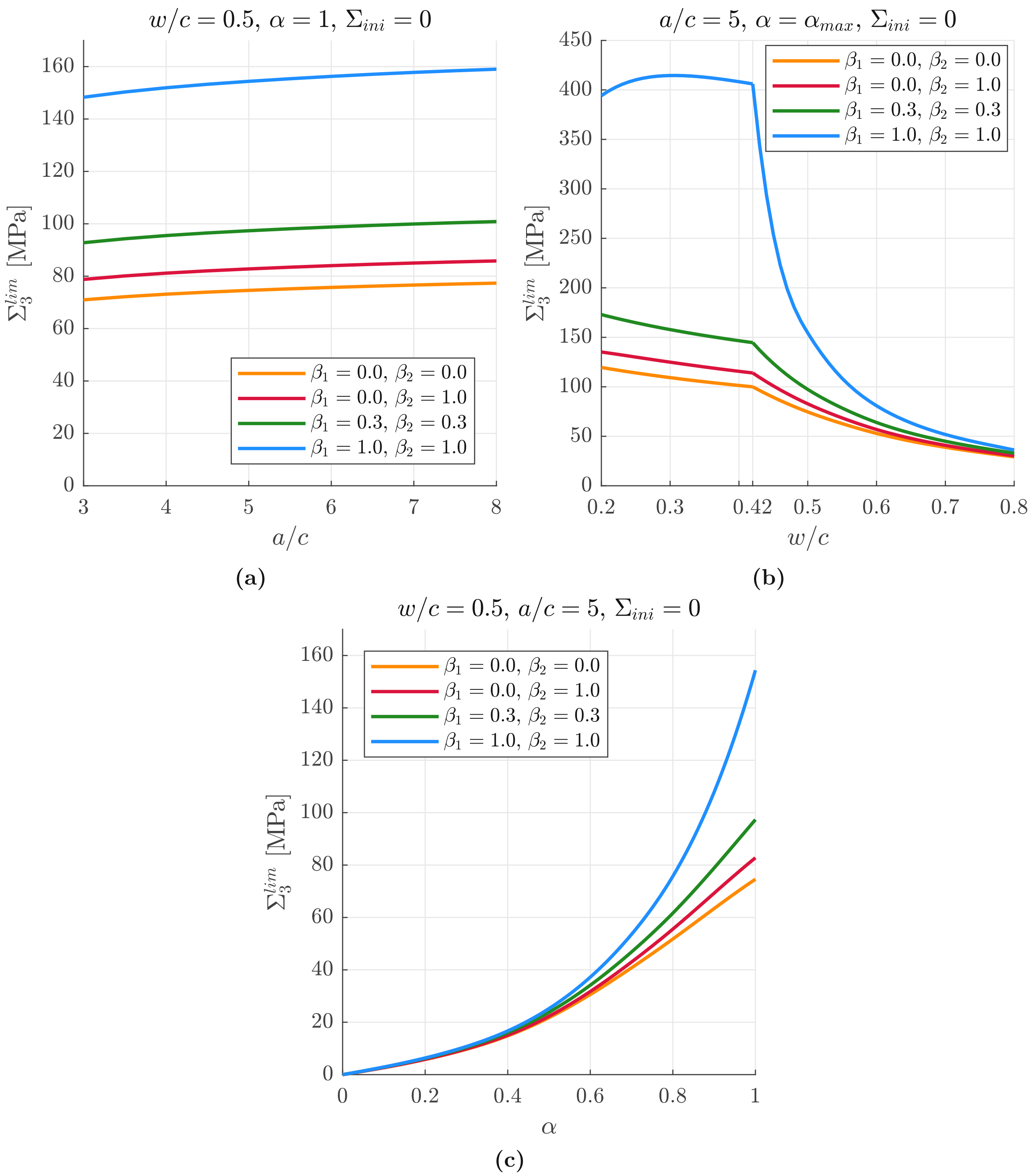

Fig. 3.5: Influence of (a) the aggregate-to-cement ratio a/c, (b) the water-to-cement ratio w/c, and (c) the hydration degree α on the elastic limit stress Σ_3^{lim} of the benchmark concrete for four different loads

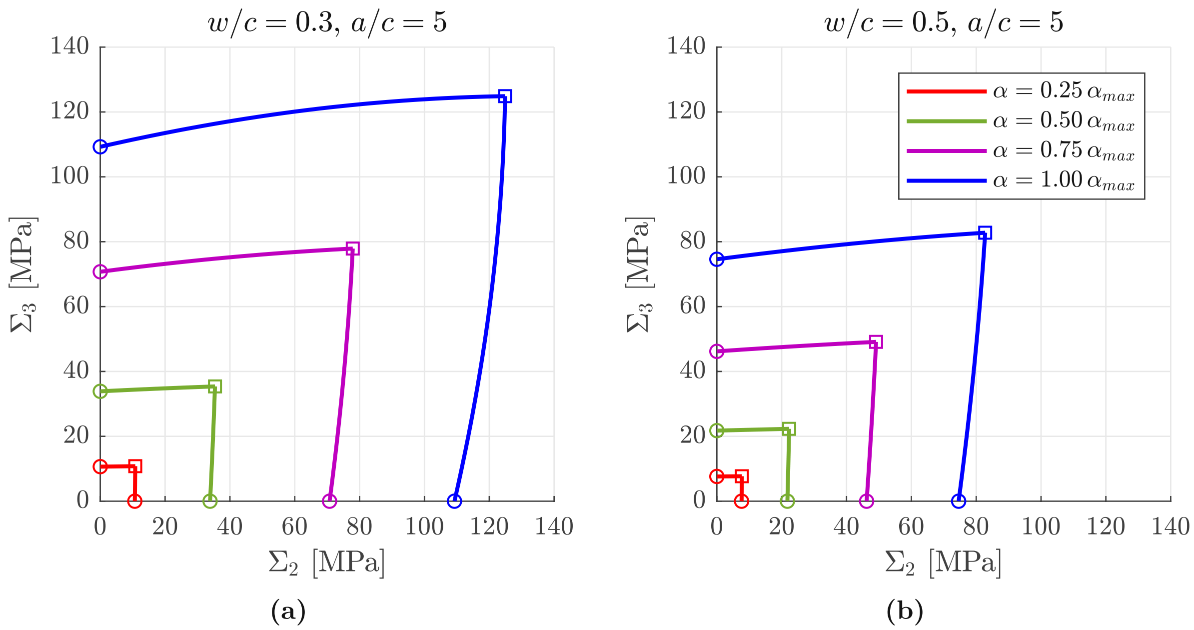

Fig. 3.6: Sensitivity analysis of the elastic limit envelope in the biaxial cross section through the principal stress space for (a) $w/c = 0.3$, $\alpha_{max} = 0.71$ and (b) $w/c = 0.5$, $\alpha_{max} = 1.00$, whereby the four envelopes correspond to four hydration degrees $\alpha \in \{0.25, 05, 0, 75, 1\}\alpha_{max}$; square points refer to hydration degree-specific symmetric biaxial elastic limit, circle points to corresponding uniaxial elastic limit

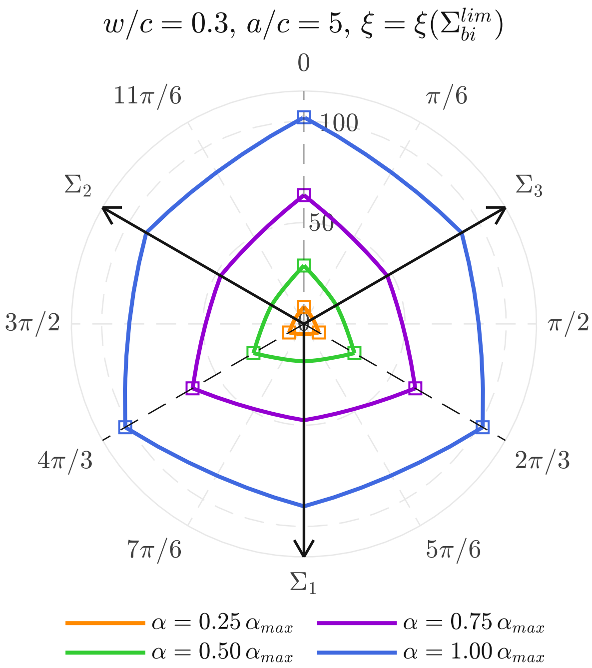

(a)

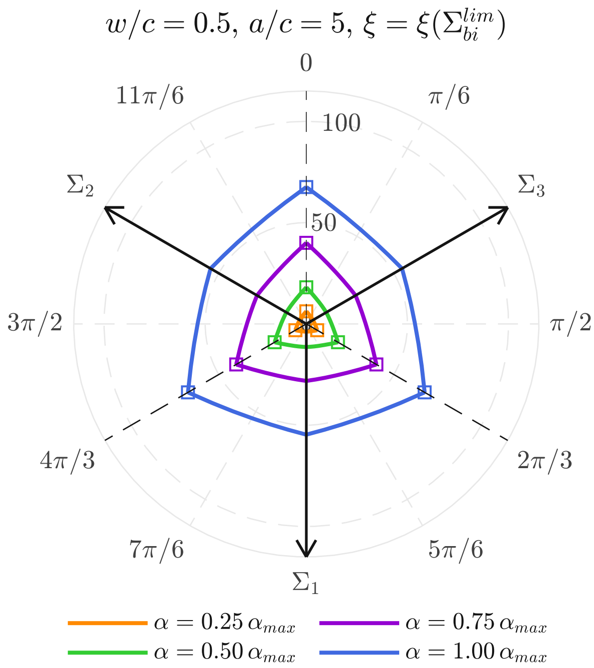

(b)

Fig. 3.7: Sensitivity analysis of the elastic limit envelope in the deviatoric cross section through the principal stress space at $\xi = \xi(\Sigma_{bi}^{lim})$ for (a) $w/c = 0.3$, $\alpha_{max} = 0.71$ and (b) $w/c = 0.5$, $\alpha_{max} = 1.00$, whereby the four envelopes correspond to four hydration degrees $\alpha \in \{0.25, 05, 0, 75, 1\}\alpha_{max}$; square points refer to hydration degree-specific symmetric biaxial elastic limits

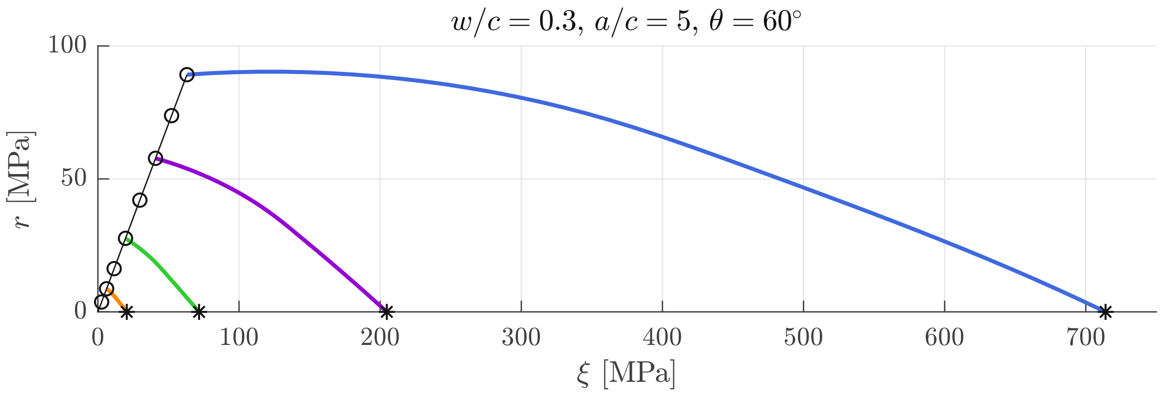

(a)

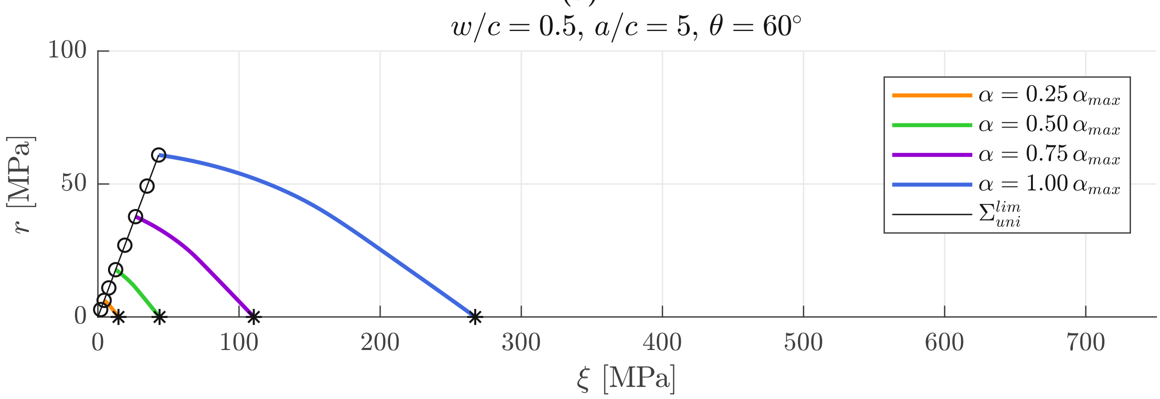

(b)

Fig. 3.8: Sensitivity analysis of the elastic limit envelope in the cross section along the hydrostatic axis at Lode angle $\theta = 60°$ for (a) $w/c = 0.3$, $\alpha_{max} = 0.71$ and (b) $w/c = 0.5$, $\alpha_{max} = 1.00$, whereby the four envelopes correspond to four hydration degrees $\alpha \in \{0.25, 05, 0, 75, 1\}\alpha_{max}$; the eight circle points refer to uniaxial elastic limits for hydration degrees $\alpha \in \{0.125,\ 0.25,\ \dots\ ,\ 1.00\}\,\alpha_{max}$ and fall on the uniaxial stress path (black solid line), and the 4 stars refer to the hydrostatic elastic limits

3.5 Comparison of model-predicted elastic limits to experimental strength values

Herein, we discuss the difference between the model-predicted elastic limits and experimentally determined strength values. Therefore, we introduce the ratio κ as the ratio between the (experimentally measured) strength Σ_3^{ult} and the corresponding (model-predicted) elastic limit Σ_3^{lim}, i.e.

$$\kappa = \frac{\Sigma_3^{ult}}{\Sigma_3^{lim}}\,. \tag{3.1}$$

The stress ratio κ quantifies the inelasticity tolerated by the material: κ close to one indicates only minor inelastic reserves, while $\kappa \gg 1$ indicates a large potential for inelastic compaction and thus a pronounced regime of pre-peak nonlinearities.

The strength values are taken from the triaxial compression tests by Imran and Pantazopoulou [24], see Table 2.2. The obtained κ values depend on the confinement, see Fig. 3.9. The strength values Σ_3^{ult} significantly increase with increasing lateral stress [24], while elastic limits Σ_3^{lim} increase only moderately, see Section 3.2. At an initial stress $\Sigma_{ini} = 20\,\mathrm{MPa}$, κ increases from 1.7 for Im 1 with $w/c = 0.4$ to $\kappa = 2.2$ for Im 2 with $w/c = 0.55$, and even to $\kappa = 3.3$ for Im 3 with $w/c = 0.75$. The individual κ values are fitted by a Power-law of the form

$$\kappa = 1 + a \left(\frac{\Sigma_{ini}}{1\,\mathrm{MPa}} \right)^b , \tag{3.2}$$

with composition-dependent Power-law coefficients a and b listed in Table 3.1. The resulting Power-law functions agree very well with the individual points, see Fig. 3.9, indicated by coefficients of determination $R^2 > 99\,\%$.

Comparing the three Power-law functions shows that κ increases with increasing w/c-ratio. This highlights that inelastic reserves are much larger for concretes with high water-to-cement ratios, driven by the ability for inelastic compaction resulting from the relatively porous microstructure. Concretes with small w/c-ratios, in turn, exhibit dense microstructures which are less susceptible to compaction. The corresponding stress ratios κ are therefore smaller. A similar conclusion has been drawn in experimental campaigns [2, 18, 48], where the authors observed that the ratio between triaxial compressive strength and the uniaxial compressive strength is much smaller for high-strength concrete (with low w/c-ratio), compared to normal-strength concrete (with moderate w/c ratio).

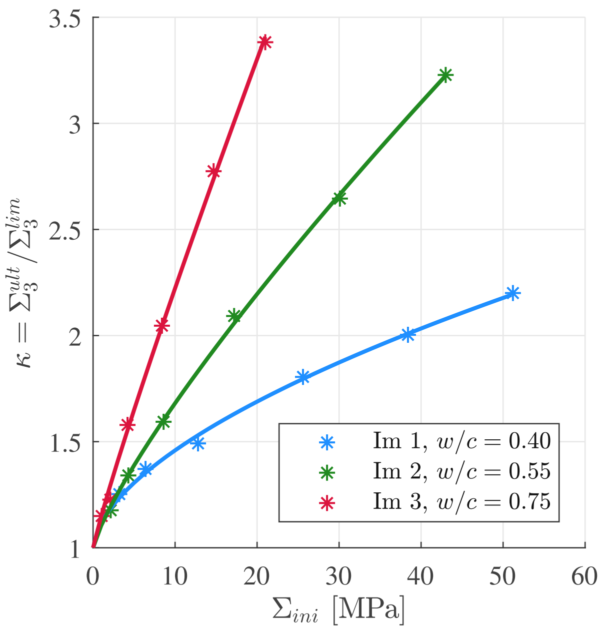

Fig. 3.9: Ratio between the measured stress at concrete failure Σ_3^{ult} [24] and the model predicted elastic limit stress Σ_3^{lim} for the concretes from Imran and Pantazopoulou [24] (see Table 2.2) and different Σ_{ini}

Tab. 3.1: Parameters for the function κ according to Eq. (3.2) for the three different mixtures tested from Imran and Pantazopoulou [24]

Mix	a	b
Im 1	0.119	0.585
Im 2	0.105	0.812
Im 3	0.149	0.913

Chapter 4

Summary and Conclusions

The multiscale model of Königsberger et al. [31] is capable of predicting the strength of normal-strength concretes subjected to *uniaxial* compression. The model suggests that macroscopic failure of concrete originates from shear failure of microscopic hydrate needles which are part of the microstructure of Interfacial Transition Zones (ITZs) located between concrete aggregates and the surrounding cement paste matrix. The model is based on scale transition methods taken from continuum micromechanics. They are used to downscale stresses imposed on macroscopic specimens of concrete, all the scales down to microscopic hydrate needles inside ITZs. This is organized in three steps. The first one refers to the quantification of volume-averaged stress and strain states inside spherical aggregates, the second step is dedicated to the position-dependent transition to the stress and strain states inside the surrounding ITZ, and the third step to the orientation-dependent stress concentration into microscopic hydrate needles. Failure of concrete under macroscopic *uniaxial* compression is related to initiation of failure of most heavily stressed hydrate needles in most unfavorably loaded regions of the ITZs, described based on a Drucker-Prager failure criterion.

Brittle material behavior of concrete observed *under* macroscopic uniaxial compression, and rather ductile behavior under macroscopic *triaxial* compression, have provided the motivation to check whether or not the described multiscale model is capable of predicting *elastic* limits of concrete under macroscopic triaxial compressive stress states. To this end, a literature survey was performed, in order to collect experimentally determined stress-strain diagrams obtained from different types of *triaxial* compression tests. The material behavior observed in such experiments can be categorized into three consecutive stages. In the first one, the stresses increase virtually linearly with increasing strains. This indicates elastic material behavior. In the second stage, the stresses increase underlinearly with increasing strains, leading to a stress maximum. The nonlinear material behavior refers to progressive damage of the microstructure. The third stage is called the “post-peak regime”, because the stresses decrease with increasing strains. This refers to the disintegration of the tested specimen. The strength of concrete under macroscopic triaxial compression is usually several times larger than the macroscopic uniaxial compressive strength. Thus, several experimental campaigns had to be stopped somewhere inside the second stage, because the testing facility was not strong enough in order to explore the failure of material.

Herein, several triaxial tests are re-analyzed, in a customized fashion, based on the multiscale model of Königsberger et al. [31]. The model accounts for the initial composition of every analyzed concrete, based on the initial water-to-cement mass ratio w/c and the initial aggregate-to-cement mass ratio a/c. These two mix-design-related properties had been provided by the experimenters in their original publications. In addition, the model accounts for the maturity of every analyzed concrete, based on a specific value of the degree of hydration α. The latter is identified such that the multiscale model reproduces the experimentally determined *uniaxial* compressive strength value. Once w/c, a/c, and α are known, the model is ready to be evaluated for any macroscopic stress state of interest. Simulating the experimentally imposed stress paths, the model is evaluated all the way up to the model-predicted elastic limit of concrete. In case of a proportional increase of a reference load, a linear problem is obtained, i.e. the elastic limit can be computed rather simply, based on the investigation of *one single* intensity of the macroscopic loading. Some experimental protocols, in turn, had been organized in two phases: a hydrostatic initial loading step followed by additional uniaxial loading. This required a much more elaborate algorithmic treatment. Because the overall linearity of the problem is limited to the first phase of the test, the stress path experimentally imposed during the second phase had to be followed in a step-by-step fashion, based on the investigation of a sequence of *many different* macroscopic stress states.

For every experiment analyzed, the model-predicted elastic limit stress was marked in the experimentally determined stress-strain diagram. This way, it was found that the transition from the first "linear elastic" stage to the subsequent stage of nonlinear stress-strain behavior can be predicted with a precision suitable for engineering design purposes. This provided the motivation to perform several types of sensitivity analyses which would be difficult to realize in laboratory testing. From the result of the described study, the following conclusions are drawn.

- Upscaling of onset of failure of hydrate needles inside ITZs allows for computing model-predicted elastic limits for multiaxially compressed concretes.
- The model-predicted elastic limits agree well with the transition from the initial "linear elastic" stage to the subsequent stage of nonlinear stress-strain behavior of concrete.
- As regards the mix-design parameters, elastic limits of well hardened concrete are the larger the smaller the initial water-to-cement mass ratio. The initial aggregate-to-cement mass ratio, in turn, has a significantly smaller influence.
- As regards the maturity of concrete, elastic limits increase significantly with increasing degree of hydration.
- Increasing lateral confinement pressure results in
  - a moderate increase of the elastic limits of young concretes and of mature concretes with large values of the initial water-to-cement mass ratio ($w/c > 0.5$),
  - a significant increase of the elastic limits of mature concretes with small values of the initial water-to-cement mass ratio ($w/c < 0.5$).

- With increasing confinement-pressure, the experimentally determined triaxial compressive strength values increase significantly. This increase is much more pronounced than the corresponding increase of the model-predicted elastic limits.
- The difference between the experimentally measured strength values and the model-predicted elastic limits increases with increasing initial water-to-cement mass ratio. Concretes with w/c values smaller than 0.55 exhibit relatively dense microstructures with only little potential for inelastic compaction. Concretes with w/c values larger than 0.55 exhibit relatively porous microstructures with much more pronounced compaction potential.

Bibliography

[1] P. Acker et al. "Micromechanical analysis of creep and shrinkage mechanisms". In: *Creep, Shrinkage and Durability Mechanics of Concrete and other quasi-brittle Materials, Cambridge, MA* (2001), pp. 15–25.

[2] F. Ansari and Q. Li. "High-strength concrete subjected to triaxial compression". In: *Materials Journal* 95.6 (1998), pp. 747–755.

[3] D. P. Bentz, O. M. Jensen, A. M. Coats, and F. P. Glasser. "Influence of silica fume on diffusivity in cement-based materials. I. Experimental and computer modeling studies on cement pastes". In: *Cement and Concrete Research* 30.6 (2000), pp. 953–962. DOI: 10.1016/S0008-8846(00)00264-7.

[4] D. P. Bentz and E. Stutzman. "Evolution of porosity and calcium hydroxide in laboratory concretes containing silica fume". In: *Cement and Concrete Research* 24.6 (1994), pp. 1044–1050. DOI: https://doi.org/10.1016/0008-8846(94)90027-2. arXiv: arXiv:1011.1669v3.

[5] Y. Benveniste. "A new approach to the application of Mori-Tanaka's theory in composite materials". In: *Mechanics of Materials* 6.2 (1987), pp. 147–157.

[6] O. Bernard, F.-J. Ulm, and E. Lemarchand. "A multiscale micromechanics-hydration model for the early-age elastic properties of cement-based materials". In: *Cement and Concrete Research* 33.9 (2003), pp. 1293–1309.

[7] O. Bernard, F. J. Ulm, and E. Lemarchand. "A multiscale micromechanics-hydration model for the early-age elastic properties of cement-based materials". In: *Cement and Concrete Research* 33.9 (2003), pp. 1293–1309.

[8] D. Bigoni and A. Piccolroaz. "Yield criteria for quasibrittle and frictional materials". In: *International Journal of Solids and Structures* 41.11 (2004), pp. 2855–2878.

[9] D. C. Candappa, J. G. Sanjayan, and S. Setunge. "Complete Triaxial Stress-Strain Curves of High-Strength Concrete". In: *Journal of Materials in Civil Engineering* 13.3 (2001), pp. 209–215. DOI: 10.1061/(asce)0899-1561(2001)13:3(209).

[10] D. Chen, X. Yu, R. Liu, S. Li, and Y. Zhang. "Triaxial mechanical behavior of early age concrete: Experimental and modelling research". In: *Cement and Concrete Research* 115.November 2017 (2019), pp. 433–444. DOI: 10.1016/j.cemconres.2018.09.013.

[11] G. Constantinides and F.-J. Ulm. “The effect of two types of C-S-H on the elasticity of cement-based materials: Results from nanoindentation and micromechanical modeling”. In: *Cement and Concrete Research* 34.1 (2004), pp. 67–80.

[12] L. Dormieux, D. Kondo, and F.-J. Ulm. “A micromechanical analysis of damage propagation in fluid-saturated cracked media”. In: *Comptes Rendus Mécanique* 334.7 (2006), pp. 440–446.

[13] W. Drugan and J. Willis. “A micromechanics-based nonlocal constitutive equation and estimates of representative volume element size for elastic composites”. In: *J. Mech. Phys. Solids* 44 (4) (1996), pp. 497–524.

[14] *Eurocode — Basis of structural design*. Standard. Wien, AT: Austrian Standards Institute, Mar. 2013.

[15] *Eurocode 2: Design of concrete structures — Part 1-1: General rules and rules for buildings*. Standard. Wien, AT: Austrian Standards Institute, Feb. 2015.

[16] A. Fritsch, L. Dormieux, and C. Hellmich. “Porous polycrystals built up by uniformly and axisymmetrically oriented needles: homogenization of elastic properties”. In: *Comptes Rendus Mécanique* 334.3 (2006), pp. 151–157.

[17] H. Geel, van. “Concrete behaviour in multiaxial compression : experimental research”. English. Proefschrift. PhD thesis. Department of the Built Environment, 1998. DOI: 10.6100/IR515170.

[18] T. Hampel, K. Speck, S. Scheerer, R. Ritter, and M. Curbach. “High-Performance Concrete under Biaxial and Triaxial Loads”. In: *Journal of Engineering Mechanics* 135.11 (2009), pp. 1274–1280. DOI: 10.1061/(asce)0733-9399(2009)135:11(1274).

[19] C. Hellmich, A. Fritsch, and L. Dormieux. “Multiscale Homogenization Theory: An Analysis Tool for Revealing Mechanical Design Principles in Bone and Bone Replacement Materials”. In: *Biomimetics – Materials, Structures and Processes: Examples, Ideas and Case Studies*. Berlin, Heidelberg: Springer Berlin Heidelberg, 2011, pp. 81–103. DOI: 10.1007/978-3-642-11934-7_5.

[20] A. Hershey. “The elasticity of an isotropic aggregate of anisotropic cubic crystals”. In: *Journal of Applied Mechanics* 21.3 (1954), pp. 236–240.

[21] R. Hill. “A self-consistent mechanics of composite materials”. In: *Journal of the Mechanics and Physics of Solids* 13.4 (1965), pp. 213–222.

[22] A. Hussein and H. Marzouk. “Behavior of High-Strength Concrete under Biaxial Stresses”. In: *ACI Materials Journal* (2000), pp. 27–36.

[23] A. Hussein. “Behaviour of high-strength concrete under biaxial loading conditions”. PhD thesis. 1998.

[24] I. Imran and S. J. Pantazopoulou. “Experimental study of plain concrete under triaxial stress”. In: *ACI Materials Journal* 93.6 (1996), pp. 589–601. DOI: 10.14359/9865.

[25] International Federation for Structural Concrete (fib). *fib Model Code for Concrete Structures*. 2010.

[26] *ISO 16204 Durability – Service life design of concrete structures*. Standard. ISO, Sept. 2012.

[27] *ISO 2394 General principles on reliability for structures*. Standard. ISO, Mar. 2015.

[28] C. Kohlhauser and C. Hellmich. “Ultrasonic contact pulse transmission for elastic wave velocity and stiffness determination: influence of specimen geometry and porosity”. In: *Eng. Struct.* 47 (2013), pp. 115–133.

[29] M. Königsberger, B. Pichler, and C. Hellmich. “Micromechanics of ITZ–Aggregate Interaction in Concrete Part I: Stress Concentration”. In: *Journal of the American Ceramic Society* 97.2 (2014), pp. 535–542.

[30] M. Königsberger. “Onset of cracking in concrete : debonding or ITZ failure? A micromechanical approach”. In: *Master Thesis* (2012).

[31] M. Königsberger, M. Hlobil, B. Delsaute, S. Staquet, C. Hellmich, and B. Pichler. “Hydrate failure in ITZ governs concrete strength: A micro-to-macro validated engineering mechanics model”. In: *Cement and Concrete Research* 103.March 2017 (2018), pp. 77–94. DOI: 10.1016/j.cemconres.2017.10.002.

[32] M. Königsberger and S. Staquet. “Micromechanical Multiscale Modeling of ITZ-Driven Failure of Recycled Concrete: Effects of Composition and Maturity on the Material Strength”. In: *Applied Sciences* 8.6 (2018). DOI: 10.3390/app8060976.

[33] E. Kröner. “Berechnung der elastischen Konstanten des Vielkristalls aus den Konstanten des Einkristalls [Computation of the elastic constants of a polycrystal based on the constants of the single crystal]”. In: *Zeitschrift für Physik A Hadrons and Nuclei* 151.4 (1958). In German, pp. 504–518.

[34] M. Liu, Y. Gao, and H. Liu. “A nonlinear Drucker–Prager and Matsuoka–Nakai unified failure criterion for geomaterials with separated stress invariants”. In: *International Journal of Rock Mechanics and Mining Sciences* 50 (2012), pp. 1–10. DOI: https://doi.org/10.1016/j.ijrmms.2012.01.002.

[35] MATLAB. *Version 9.3.0 (R2017b)*. Natick, Massachusetts: The MathWorks Inc., 2017.

[36] T. Mori and K. Tanaka. “Average stress in matrix and average elastic energy of materials with misfitting inclusions”. In: *Acta Metallurgica* 21.5 (1973), pp. 571–574.

[37] V. Nežerka, P. Bílý, V. Hrbek, and J. Fládr. “Impact of silica fume, fly ash, and metakaolin on the thickness and strength of the ITZ in concrete”. In: *Cement and Concrete Composites* 103.January (2019), pp. 252–262. DOI: 10.1016/j.cemconcomp.2019.05.012.

[38] B. Pichler and C. Hellmich. “Upscaling quasi-brittle strength of cement paste and mortar: A multi-scale engineering mechanics model”. In: *Cement and Concrete Research* 41 (2011), pp. 467–476.

[39] B. Pichler, C. Hellmich, and J. Eberhardsteiner. "Spherical and acicular representation of hydrates in a micromechanical model for cement paste: prediction of early-age elasticity and strength". In: *Acta Mechanica* 203.3 (2009), pp. 137–162.

[40] B. Pichler, C. Hellmich, J. Eberhardsteiner, J. Wasserbauer, P. Termkhajornkit, R. Barbarulo, and G. Chanvillard. "Effect of gel-space ratio and microstructure on strength of hydrating cementitious materials: An engineering micromechanics approach". In: *Cement and Concrete Research* 45 (2013), pp. 55–68.

[41] C. Poinard, E. Piotrowska, Y. Malecot, L. Daudeville, and E. N. Landis. "Compression triaxial behavior of concrete: the role of the mesostructure by analysis of X-ray tomographic images". In: *European Journal of Environmental and Civil Engineering* 16.sup1 (June 2012), s115–s136. DOI: 10.1080/19648189.2012.682458.

[42] T. Powers and T. Brownyard. "Studies of the physical properties of hardened Portland cement paste". In: *Research Laboratories of the Portland Cement Association Bulletin* 22 (1948), pp. 101–992.

[43] J. Salençon. *Handbook of continuum mechanics: general concepts, Thermoelasticity.* Springer Verlag, 2001.

[44] E. Sarris and G. Constantinides. "Finite element modeling of nanoindentation on C–S–H: Effect of pile-up and contact friction". In: *Cement and Concrete Composites* 36 (2013), pp. 78–84.

[45] D. Sfer, I. Carol, R. Gettu, and G. Etse. "Study of the behavior of concrete under triaxial compression". In: *Journal of Engineering Mechanics* 128.2 (2002), pp. 156–163. DOI: 10.1061/(ASCE)0733-9399(2002)128:2(156).

[46] J. Vorel, V. Šmilauer, and Z. Bittnar. "Multiscale simulations of concrete mechanical tests". In: *Journal of Computational and Applied Mathematics* 236.18 (2012), pp. 4882–4892. DOI: 10.1016/j.cam.2012.01.009.

[47] X. H. Vu, Y. Malecot, and L. Daudeville. "Strain measurements on porous concrete samples for triaxial compression and extension tests under very high confinement". In: *Journal of Strain Analysis for Engineering Design* 44.8 (2009), pp. 633–657. DOI: 10.1243/03093247JSA547.

[48] Y.-B. Wang, J. Y. Liew, S. C. Lee, and D. X. Xiong. "Experimental Study of Ultra-High-Strength Concrete under Triaxial Compression." In: *Aci Materials Journal* 113.1 (2016).

[49] J. Wastiels. "Behaviour of concrete under multiaxial stresses – A review". In: *Cement and Concrete Research* 9.1 (1979), pp. 35–44. DOI: 10.1016/0008-8846(79)90092-9.

[50] A. Zaoui. "Continuum Micromechanics: Survey". In: *Journal of Engineering Mechanics* 128.8 (2002), pp. 808–816.

Appendix A

Homogenized stiffness tensors and stress concentrations tensors

Herein, we describe the stiffness homogenization of concrete and the stress concentration tensors used for downscaling the macrostresses into spatial average hydrate stresses. First, the hydrate foam [Fig. 2.1(c)] is homogenized by means of the self consistent scheme [20, 21, 33], which is extended for infinitely many phases [16]. This self consistent scheme is appropriate due to the polycrystalline interaction between the hydrate needle phase and capillary pore phase and yields an implicit expression of the homogenized stiffness tensor of the hydrate foam $\mathbb{C}_{hf}$, reading as [39]:

$$\begin{aligned}\mathbb{C}_{hf} = &\Bigg(f^{hf}_{pore}\mathbb{C}_{pore} : \Big\{\mathbb{I} + \mathbb{P}^{hf}_{sph} : [\mathbb{C}_{pore} - \mathbb{C}_{hf}]\Big\}^{-1} \\ &+ f^{hf}_{hyd}\mathbb{C}_{hyd} : \int_0^{2\pi}\int_0^{\pi} \Big\{\mathbb{I} + \mathbb{P}^{hf}_{cyl}(\varphi,\vartheta) : [\mathbb{C}_{hyd} - \mathbb{C}_{hf}]\Big\}^{-1} \frac{\sin\vartheta}{4\pi}\mathrm{d}\vartheta\,\mathrm{d}\varphi \Bigg) : \\ &\Bigg(f^{hf}_{pore}\Big\{\mathbb{I} + \mathbb{P}^{hf}_{sph} : [\mathbb{C}_{pore} - \mathbb{C}_{hf}]\Big\}^{-1} \\ &+ f^{hf}_{hyd}\int_0^{2\pi}\int_0^{\pi} \Big\{\mathbb{I} + \mathbb{P}^{hf}_{cyl}(\varphi,\vartheta) : [\mathbb{C}_{hyd} - \mathbb{C}_{hf}]\Big\}^{-1} \frac{\sin\vartheta}{4\pi}\mathrm{d}\vartheta\,\mathrm{d}\varphi \Bigg)^{-1} .\end{aligned} \tag{A.1}$$

In Eq. (A.1), f^{hf}_{hyd} and f^{hf}_{pore} are the hydrate foam-related volume fractions of the hydrate needles and the pores, respectively, according to Eq. (2.4). $\mathbb{C}_{hyd}$ and $\mathbb{C}_{pore}$ denote the phase elasticity tensor of the hydrate needles and the pores, respectively [see Eq. (2.6)]. $\mathbb{P}^{hf}_{cyl}$ and $\mathbb{P}^{hf}_{sph}$ denote the phase-specific Hill tensors. They incorporate the cylindrical shape of the hydrate needles ($\mathbb{P}^{hf}_{cyl}$) and the spherical shapes of the pores ($\mathbb{P}^{hf}_{sph}$), see Pichler et al. [39]. The orientation of the hydrate needle is described by the zenith ϑ and azimuth φ angles according to Fig. 2.2(b). At the RVE of cement paste, clinker is embedded in a hydrate foam matrix, rendering the Mori-Tanaka scheme [5, 36] appropriate for homogenization. The homogenized stiffness tensors of cement paste $\mathbb{C}_{cp}$ then reads as [39]

$$\begin{aligned}\mathbb{C}_{cp} = &\left(f_{hf}^{cp}\, \mathbb{C}_{hf} + f_{clin}^{cp}\, \mathbb{C}_{clin} : \left\{ \mathbb{I} + \mathbb{P}_{sph}^{hf} : [\mathbb{C}_{clin} - \mathbb{C}_{hf}] \right\}^{-1} \right) : \\ &\left(f_{hf}^{cp}\, \mathbb{I} + f_{clin}^{cp} \left\{ \mathbb{I} + \mathbb{P}_{sph}^{hf} : [\mathbb{C}_{clin} - \mathbb{C}_{hf}] \right\}^{-1} \right)^{-1} ,\end{aligned} \tag{A.2}$$

where f_{clin}^{cp} and f_{hf}^{cp} is the cement paste-related clinker and hydrate foam matrix volume fraction, respectively, according to Eq. (2.3) and $\mathbb{C}_{clin}$ denotes the phase elasticity tensor of the clinker grains. As for the homogenization of the concrete RVE, the Mori-Tanaka scheme [5, 36] is again appropriate since the aggregates are embedded in the cement paste matrix, see Fig. 2.1(a). The resulting homogenized stiffness tensor of concrete, $\mathbb{C}_{con}$, reads as [40]

$$\begin{aligned}\mathbb{C}_{con} = &\left(f_{cp}^{con}\, \mathbb{C}_{cp} + f_{agg}^{con}\, \mathbb{C}_{agg} : \left\{ \mathbb{I} + \mathbb{P}_{sph}^{cp} : [\mathbb{C}_{agg} - \mathbb{C}_{cp}] \right\}^{-1} \right) : \\ &\left(f_{cp}^{con}\, \mathbb{I} + f_{agg}^{con} \left\{ \mathbb{I} + \mathbb{P}_{sph}^{cp} : [\mathbb{C}_{agg} - \mathbb{C}_{cp}] \right\}^{-1} \right)^{-1} ,\end{aligned} \tag{A.3}$$

whereby f_{agg}^{con} and f_{cp}^{con} denotes the concrete-related aggregate and cement paste volume fraction, respectively (see Eq. (2.2)) and $\mathbb{P}_{sph}^{con}$ stands for the cement paste-related Hill tensor describing spherical inclusions.

Downscaling of the macrostresses to the spatial average of hydrate stresses calls for the stress concentration tensors $\mathbb{B}_{agg}^{con}$ and $\mathbb{B}_{cp}^{agg}$, see Eq. (2.7). The isotropic concrete-to-aggregate stress concentration tensor $\mathbb{B}_{agg}^{con}$ is given by [29]

$$\begin{aligned}\mathbb{B}_{agg}^{con} = &\,\mathbb{C}_{agg} : \left\{ \mathbb{I} + \mathbb{P}_{sph}^{cp} : [\mathbb{C}_{agg} - \mathbb{C}_{cp}] \right\}^{-1} : \\ &\left(f_{cp}^{con}\, \mathbb{I} + f_{agg}^{con} \left\{ \mathbb{I} + \mathbb{P}_{sph}^{cp} : [\mathbb{C}_{agg} - \mathbb{C}_{cp}] \right\}^{-1} \right)^{-1} : (\mathbb{C}_{con})^{-1} .\end{aligned} \tag{A.4}$$

Finally, the non-zero components of the aggregate-to-cement paste stress concentration tensor $\mathbb{B}_{cp}^{agg}$ are given in the spherical base frame vectors $\underline{e}_r$, $\underline{e}_\psi$, $\underline{e}_\omega$ according to Fig. 2.2(a) [29]:

$$\begin{aligned}
B_{cp,rrrr}^{agg} &= 1 \\
B_{cp,\psi\psi\psi\psi}^{agg} &= B_{cp,\omega\omega\omega\omega}^{agg} = \mu_{cp} \left(3\, k_{agg} k_{cp} + 2\, k_{agg} \mu_{cp} + 2\, k_{cp} \mu_{agg} \right) / \Delta \\
B_{cp,\psi\psi\omega\omega}^{agg} &= B_{cp,\omega\omega\psi\psi}^{agg} = 2\, \mu_{cp} \left(k_{cp} \mu_{agg} - k_{agg} \mu_{cp} \right) / \Delta \\
B_{cp,\psi\psi rr}^{agg} &= B_{cp,\omega\omega rr}^{agg} = \left[3\, k_{agg} k_{cp} \left(\mu_{agg} - \mu_{cp} \right) - 2\, \mu_{agg} \mu_{cp} \left(k_{agg} - k_{cp} \right) \right] / \Delta \\
B_{cp,r\psi r\psi}^{agg} &= B_{cp,r\omega r\omega}^{agg} = \frac{1}{2} \\
B_{cp,\psi\omega\psi\omega}^{agg} &= \frac{\mu_{cp}}{2\, \mu_{agg}}
\end{aligned} \tag{A.5}$$

with $\Delta = k_{agg} \mu_{agg} \left(3\, k_{cp} + 4\, \mu_{cp} \right)$ and with the symmetries $B_{cp,ijkl}^{agg} = B_{cp,jikl}^{agg} = B_{cp,ijlk}^{agg} = B_{cp,jilk}^{agg}$.

Appendix B

Haigh-Westergaard coordinate system

The Haigh-Westergaard coordinate system is well suited for depicting and discussing multiaxial stress states. It is a cylindrical coordinate system, whereby the cylinder axis is equal to the hydrostatic axis, i.e. the space diagonal of the principal stress space (see Fig. B.1). On the hydrostatic axis, the three principal stresses are equal ($\Sigma_1 = \Sigma_2 = \Sigma_3$). The plane which is normal to the hydrostatic axis is called deviatoric plane (see Fig. B.1) [30, 34]. Any stress state

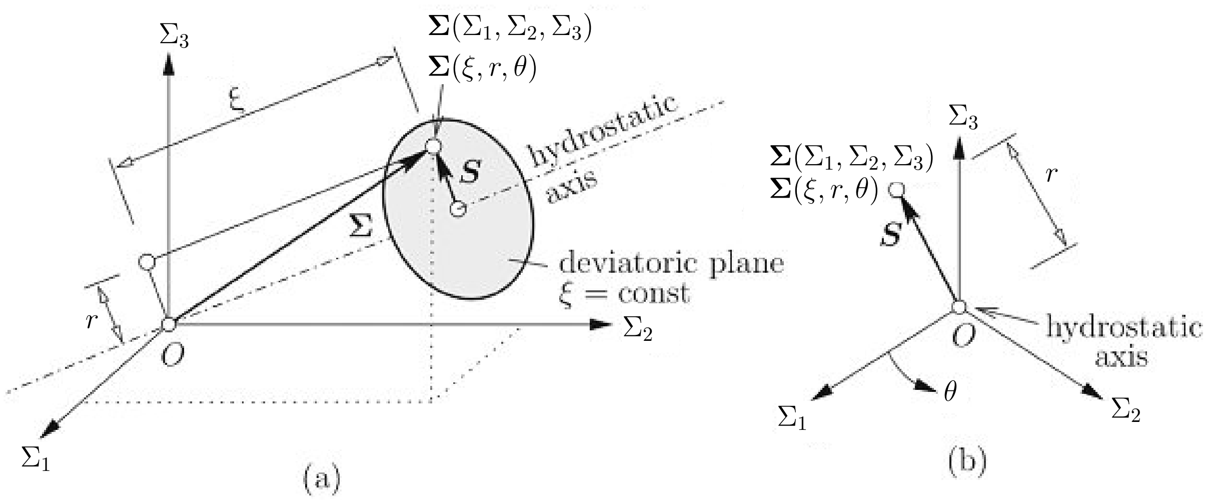

Fig. B.1: (a) Macroscopic stress tensor with the Haigh-Westergaard coordinates, (b) deviatoric plane with the stress deviator $\boldsymbol{S}$ [30]; note that in this figure positive values are tension.

$\boldsymbol{\Sigma}(\Sigma_1, \Sigma_2, \Sigma_3)$ can then be described by means of three Haigh-Westergaard coordinates $\boldsymbol{\Sigma}(\xi, r, \theta)$: a hydrostatic coordinate ξ, a deviatoric coordinate r, and the Lode angle θ. The hydrostatic coordinate ξ is the projection length of $\boldsymbol{\Sigma}$ on the hydrostatic axis, r is the projection length of $\boldsymbol{\Sigma}$ on the deviatoric plane, labeled $\boldsymbol{S}$ in Fig. B.1, and θ is the angle between $\boldsymbol{S}$ and the projection of the coordinate axis Σ_1.

Coordinate transformations from the Cartesian base frame with coordinates Σ_1, Σ_2, Σ_3 to the cylindrical base frame with coordinates ξ, r, θ are discussed. The Haigh-Westergaard coordinates of any stress tensor $\boldsymbol{\Sigma}$ follow from [43]

$$\xi = \frac{1}{\sqrt{3}} I_1^{\boldsymbol{\Sigma}}\,, \quad r = \sqrt{2\, J_2^{\boldsymbol{S}}}\,, \quad \cos(3\theta) = \frac{3\sqrt{3}}{2} \frac{J_3^{\boldsymbol{S}}}{(J_2^{\boldsymbol{S}})^{3/2}}\,, \tag{B.1}$$

whereby invariants $I_1^{\boldsymbol{\Sigma}}$, $J_2^{\boldsymbol{S}}$, and $J_3^{\boldsymbol{S}}$ read as

$$I_1^{\boldsymbol{\Sigma}} = \mathrm{tr}\,\boldsymbol{\Sigma}\,, \quad J_2^{\boldsymbol{S}} = \frac{1}{2}\,\boldsymbol{S} : \boldsymbol{S}\,, \quad J_3^{\boldsymbol{S}} = \frac{1}{3}\,(\boldsymbol{S} \cdot \boldsymbol{S}) : \boldsymbol{S} \tag{B.2}$$

and whereby $\boldsymbol{S}$ denotes the stress deviator, defined as

$$\boldsymbol{S} = \boldsymbol{\Sigma} - \frac{I_1^{\boldsymbol{\Sigma}}}{3}\,\mathbf{1}\,. \tag{B.3}$$

Cartesian coordinates follow from their Haigh-Westergaard counterparts as

$$\begin{aligned}
\Sigma_1 &= \frac{1}{3}\left[\sqrt{a}\,\cos\,(b+\frac{\pi}{6}) + \sqrt{3\,a\left(\sin\,(b+\frac{\pi}{6})\right)^2} + I_1^{\boldsymbol{\Sigma}}\right] \\
\Sigma_2 &= \frac{1}{3}\left[\sqrt{a}\,\cos\,(b+\frac{\pi}{6}) - \sqrt{3\,a\left(\sin\,(b+\frac{\pi}{6})\right)^2} + I_1^{\boldsymbol{\Sigma}}\right] \\
\Sigma_3 &= -\frac{1}{3}\left[2\,\sqrt{a}\,\cos\,(b+\frac{\pi}{6}) - I_1^{\boldsymbol{\Sigma}}\right]\,,
\end{aligned} \tag{B.4}$$

whereby auxiliary variables a and b are given in terms of invariants $I_1^{\boldsymbol{\Sigma}}$, $I_2^{\boldsymbol{\Sigma}}$, and $I_3^{\boldsymbol{\Sigma}}$ as

$$a = (I_1^{\boldsymbol{\Sigma}})^2 - 3\,I_2^{\boldsymbol{\Sigma}} \tag{B.5}$$

and

$$b = \frac{1}{3}\arcsin\frac{2\,(I_1^{\boldsymbol{\Sigma}})^3 - 9\,I_1^{\boldsymbol{\Sigma}}\,I_2^{\boldsymbol{\Sigma}} + 27\,I_3^{\boldsymbol{\Sigma}}}{2\,a^{3/2}}\,. \tag{B.6}$$

The invariants, can be given in terms of Haigh-Westergaard coordinates as

$$I_1^{\boldsymbol{\Sigma}} = \xi\sqrt{3}\,, \quad I_2^{\boldsymbol{\Sigma}} = (I_1^{\boldsymbol{\Sigma}})^2\,\frac{1}{3} - J_2^{\boldsymbol{S}}\,, \quad I_3^{\boldsymbol{\Sigma}} = J_3^{\boldsymbol{S}} + I_1^{\boldsymbol{\Sigma}} + \frac{1}{3}\,I_2^{\boldsymbol{\Sigma}} - \frac{2}{27}\,(I_1^{\boldsymbol{\Sigma}})^3\,, \tag{B.7}$$

with

$$J_2^{\boldsymbol{S}} = \frac{1}{2}\,r^2\,, \quad J_3^{\boldsymbol{S}} = \cos\,(3\theta)\,\frac{2}{3\sqrt{3}}\,\sqrt{J_2^{\boldsymbol{S}}}\,. \tag{B.8}$$

The eigenvalues of the stress tensor can be ordered in any way, therefore each stress state is symmetric to the projection of the principal stress on the deviatoric plane [8]. This implies that any stress states can be produced by mirroring and rotating the stress states for the Lode angles between 0° and 60°. Considering this effect in the computation of the failure surface reduces calculation time, since it is enough to evaluate 1/6 of the failure surface with the micromechanics model.

Appendix C

Comparison of model-predicted elastic limits to experimental stress-strain curves of concretes with silica fume

Hussein and Marzouk [22, 23] tested additional to the normal-strength concrete Hu 1, high-strength concrete Hu 2, and ultra-high-strength concrete Hu 3, both of which contain silica fume. The addition of silica fume is considered by introducing the water-to-cement-and-silica-fume ratio of $w/(c+s_f) = 0.28$ and $w/(c+s_f) = 0.23$ for Hu 2 and Hu 3, respectively, which is used for calculation of phase volume fraction instead of the w/c ratio. The testing characteristics, such as load path, geometry, age, and friction reduction are the same as for the normal-strength concrete, described in Section 2.2. The aggregate-to-cement ratio and the hydration degree as well as all the other properties are listed in Table C.1.

Tab. C.1: Properties of the concretes tested in the experiments

Source	Mix	$w/(c+s_f)$ [–]	a/c [–]	Geometry [mm]	Age [months]	f_c^{uni} [MPa]	α [–]	Σ_{ini} [MPa]	β_1 [–]	β_2 [–]
[22, 23]	Hu 2	0.28	3.69	$a \times b \times c$ $40 \times 150 \times 150$	≥ 2	76.60	0.53	0.0	0.00	$0.20 - 1.00$
	Hu 3	0.23	3.18			100.08	0.50	0.0	0.00	$0.20 - 1.00$

The model predicted elastic limit generally overestimates the elastic limit in the stress-strain diagrams from Hussein and Marzouk [22, 23] for symmetric biaxial compression, see Fig. C.1, most likely due to the additional silica fume. Silica fume reduces the porosity of the ITZ and therefore strengthens it [37], as shown by scanning electron microscopy [4] and high resolution electron probe micro-analysis [3]. Since the hydration degree is back-identified from the measured uniaxial compressive strength of concrete with silica fume [22, 23], the hydration degree is overestimated, leading to the aforementioned overestimation of the elastic limit. Moreover, the model-predicted elastic limit reaches its maximum for symmetric biaxial compression ($\beta_1 = \beta_2$), whereas the maximum is at $\beta_2 = 0.5$ in the experimentally determined stress-strain diagram of Hu 2 and Hu 3, see Fig. C.1.

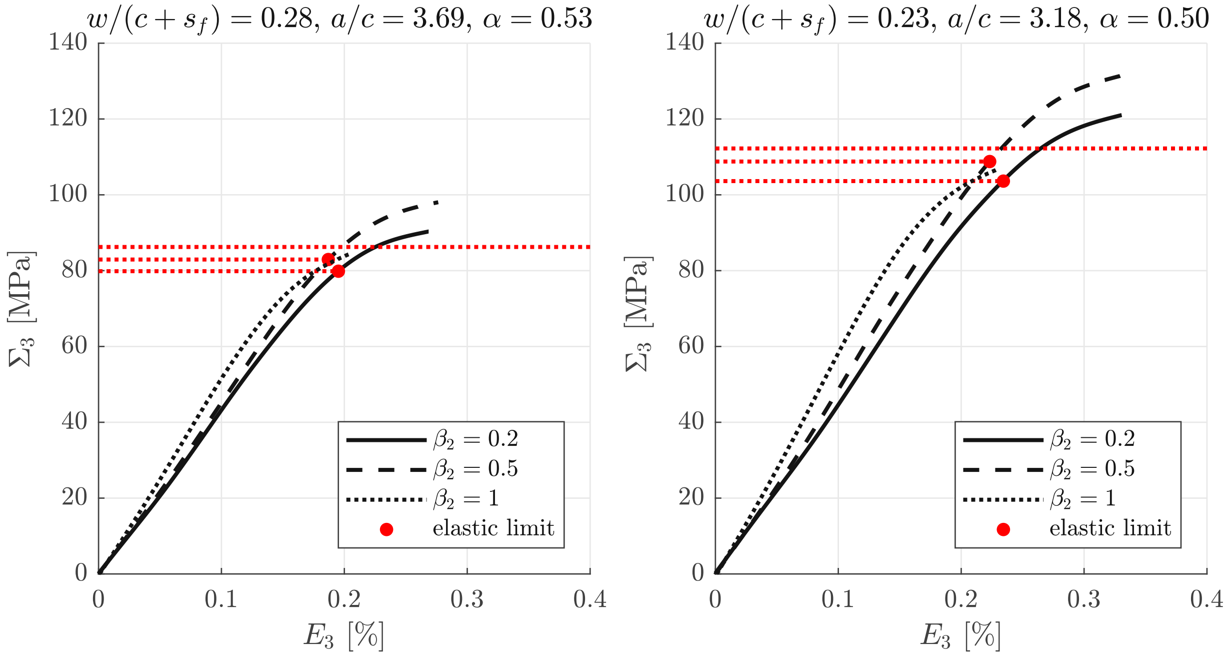

(a) High-strength concrete (Hu 2) experimental data from Hussein [23]

(b) Ultra-high-strength concrete (Hu 3) experimental data from Hussein and Marzouk [22]

Fig. C.1: Model validation: Comparison of predicted elastic limits with experimental stress-strain curves from Hussein and Marzouk [22, 23]; the load path is characterized by specifying Eq. (2.13) for $\Sigma_{ini} = 0$, $\beta_1 = 0$, and $\beta_2 > 0$ (biaxial compression)

Appendix D

Model implementation in Matlab environment

Herein, we display Matlab [35] scripts and functions to calculate and plot the elastic limit surface, for the example of the benchmark concrete introduced in Section 3.3. The calculation of the elastic limit for different stress states is shown in the script labeled D.1. Therein, the stress states are defined in Haigh-Westergaard coordinates ξ, r and θ, where ξ and r are expressed with the angle γ reading as:

$$\tan(\gamma) = \frac{\xi}{r}\,. \tag{D.1}$$

Defining the stress state in Haigh-Westergaard coordinates helps plotting the 3D elastic limit failure surface and its cross sections. To plot the biaxial elastic limit plane the stress states are defined in the Cartesian coordinates with the parameter β_1 and β_2 [see Eq. (2.13)]. This calculation of the elastic limit in Cartesian coordinates is done in Code D.2. The 3D elastic limit surface Fig. 3.3, the biaxial plane Fig. 3.4(a), the deviatoric plane Fig. 3.4(b) and the cross section along the hydrostatic axis Fig. 3.4(c) are plotted with the Code D.3.

The main functions used in the Codes D.1 to D.3 are given in Codes D.4 to D.11. The first function, which calculates the difference quotients in Eq. (2.8) and Eq. (2.9) as well as the homogenized stiffness tensor of hydrate foam [Eq. (A.1)] and cement paste [Eq. (A.2)], is shown in Code D.4. Homogenization of concrete [Eq. (A.3)] as well as stress concentration into the aggregate [Eq. (A.4)] and further stress concentration into the cement paste [Eq. (A.5)] are computed with Code D.5 and Code D.6. An auxiliary tensor for the strain concentration tensor of the hydrate needle phase is calculated with Code D.7. The calculation of the phase elasticity tensor from the bulk moduli and shear moduli [Eq. (2.6)] as well as the calculation of the bulk and shear moduli from the elasticity tensor are written in Code D.8 and Code D.9, respectively. Coordinate transformation from Cartesian coordinates to Haigh-Westergaard coordinates and vice versa (see Appendix B), is done with the functions in Code D.10 and Code D.11, respectively.

Code D.1: Calculation of the elastic limit in Haigh-Westergaard coordinates

```
%% Phase specific input parameter
number_of_alpha=1;
wc_list=0.5; % Water-to-cement mass ratio
ac_list=3; % Aggregate-to-cement mass ratio
alpha_list=1; % Hydration degree
```

```
tolerance = 1e-10;
tolerance_2 = 1e-8;
rho.H2O=1000; rho.hyd=2073; rho.cem=3150; rho.agg=2650; % Densities [kg/m3]
kagg=35.35; muagg=29.91; % Bulk and shear modulus of aggregates [GPa]

% Initializing precalculation
diffQ(numel(wc_list),number_of_alpha).vol=[];
diffQ(numel(wc_list),number_of_alpha).dev=[];
Chom(numel(ac_list),numel(wc_list),number_of_alpha).hf=[];
Chom(numel(ac_list),numel(wc_list),number_of_alpha).cp=[];

%% Precalculate diffQ and homogenized stiffness tensor for the hydrate ...
    foam and the cement paste Chom
for wcit=1:length(wc_list)
    wc=wc_list(wcit);
    for xiit=1:length(alpha_list)
        xi_p=alpha_list(xiit);
            if isempty(diffQ(wcit,xiit).vol)
                [diffQ(wcit,xiit),Chom(1,wcit,xiit)] = ...
                    fun_CCR2018_precalc(wc, xi_p, rho, tolerance, ...
                    tolerance_2); % see Code D.4
            end
    end
end


%% Hydrate needle parameter
% Mohr-Coulomb
phi_hyd_degree=12; % Friction angle [degree]
c_hyd=0.050; % Cohesion [GPa]
phi_hyd=phi_hyd_degree*pi/180; % Friction angle [rad]
fc_MC=2*c_hyd*cos(phi_hyd)/(1-sin(phi_hyd)); % Strength
Ehyd=29.15786664; % Young's modulus
nuhyd=0.24; % Poisson's ratio
khyd=Ehyd/3/(1-2*nuhyd); % Bulk modulus
muhyd=Ehyd/2/(1+nuhyd); % Shear modulus

% Drucker Prager (based on Mohr-Coulomb parameters)
alpha_DP=sqrt(3)*fc_MC*tan(phi_hyd)/(3*c_hyd+fc_MC*tan(phi_hyd));
k_DP=c_hyd*alpha_DP/tan(phi_hyd);
fc_DP=3*k_DP/(sqrt(3)-alpha_DP); % Strength


%% Define stress state part 1
% The applied stress state is defined in Haigh-Westergaard coordinates

lode_list=[linspace(0.001,30,6),linspace(31,59.9,6)]*pi/180; % List of ...
    Lode angles between 0 and 60 degrees, with which all possible stress ...
    states can be represented by rotation and mirroring of the results.
```

```
laenge_gamma_list=14; % Length of gamma for initialization

%% Initializing elastic limit calculation

Chom(numel(ac_list),numel(wc_list),numel(alpha_list(1,:))).con=zeros(6);
B_agg=cell(numel(ac_list),numel(wc_list),numel(alpha_list(1,:)));

r_result=zeros(laenge_gamma_list,numel(lode_list));
xi_result=zeros(laenge_gamma_list,numel(lode_list));
phi_result=zeros(laenge_gamma_list,numel(lode_list));
theta_result=zeros(laenge_gamma_list,numel(lode_list));
psi_result=zeros(laenge_gamma_list,numel(lode_list));
omega_result=zeros(laenge_gamma_list,numel(lode_list));

sig1_result=zeros(laenge_gamma_list,numel(lode_list));
sig2_result=zeros(laenge_gamma_list,numel(lode_list));
sig3_result=zeros(laenge_gamma_list,numel(lode_list));

r_mix=cell(length(wc_list),length(alpha_list(1,:)),numel(ac_list));
xi_mix=cell(length(wc_list),length(alpha_list(1,:)),numel(ac_list));
sig1_mix=cell(length(wc_list),length(alpha_list(1,:)),numel(ac_list));
sig2_mix=cell(length(wc_list),length(alpha_list(1,:)),numel(ac_list));
sig3_mix=cell(length(wc_list),length(alpha_list(1,:)),numel(ac_list));
phi_mix=cell(length(wc_list),length(alpha_list(1,:)),numel(ac_list));
theat_mix=cell(length(wc_list),length(alpha_list(1,:)),numel(ac_list));
psi_mix=cell(length(wc_list),length(alpha_list(1,:)),numel(ac_list));
omega_mix=cell(length(wc_list),length(alpha_list(1,:)),numel(ac_list));


%% Calculation of the elastic limit

% Loop over the concrete mixtures
for wcit=1:length(wc_list)
    wc=wc_list(wcit);
    for xiit=1:length(alpha_list)
        xi_p=alpha_list(xiit);
        for acit=1:numel(ac_list)
            ac=ac_list(acit);

            % Loop over the different stress states
            for lodeit=1:numel(lode_list) % loop over the Lode angel
                % Define stress state part 1
                % Gamma is defined as: tan(gamma) = xi / r
                gamma_min=fitresult_min_alpha(lode_list); % The Lode Angle ...
                    specific minimum gamma, where the stress state is still ...
                    pure compression, which corresponds to the uniaxial ...
                    stress state at the Lode angle = 60 degree and biaxial ...
                    compression for the other lode angles
```

```
        gamma_list= [linspace(gamma_min(lodeit)*180/pi,60,4), ... linspace(65,75.0,5), linspace(78,89.0,5)] * pi/180;
        r_list=cos(gamma_list);
        xi_list=-sin(gamma_list);

        for gammait=1:numel(gamma_list)% loop over gamma

            lode=lode_list(lodeit);
            r=r_list(gammait);
            xi=xi_list(gammait);

            % Convert stress state in Haigh-Westergaard
            % Coordinate system into Cartesian coordinate system
            [sig_1,sig_2,sig_3] = ...
                fun_haigh_westergaard_to_cartesian(xi,r,lode); % ... see Code D.11


            SI_macro=[sig_1,sig_2,sig_3,0,0,0]'; % Applied ... macroscopic load in the Cartesian e1,e2,e3 base

            SI_DP=1000; SI_vM=1000; SI_MC=1000; % [GPa] % ... Initialization

            % Homogenization of the concrete
            Chom(acit,wcit,xiit).hf=Chom(1,wcit,xiit).hf;
            Chom(acit,wcit,xiit).cp=Chom(1,wcit,xiit).cp;
            [Chom(acit,wcit,xiit).con,B_agg{acit,wcit,xiit}] = ...
                fun_CCR2018_conhom(ac, wc, rho, ...
                Chom(1,wcit,xiit).cp, kagg, muagg); % see Code D.5

            % First order stress concentration to ITZ
            [~,~,k_ITZ,mu_ITZ]=fun_Enu_from_C( Chom(acit, wcit, ... xiit).cp); % see Code D.9
            C_ITZ=fun_Cfromkmu(k_ITZ,mu_ITZ); see Code D.8
            BITZagg_sph = fun_BITZagg(kagg,k_ITZ,muagg,mu_ITZ); % ... see Code D.6

            % Define angles steps
            stepsangle=45;
            angle_dis=0:pi/(2*(stepsangle-1)):pi/2;

            % Angles of the hydrate needle in the space
            % Because of symmetry it is enough to calculate points ... in the hemisphere
            for thetait=1:stepsangle
                theta=angle_dis(thetait);
                for phiit=1:stepsangle
                    phi=angle_dis(phiit)*2;

```

```
Q4=fun_Q4_bp(phi,theta);
Q4t=transpose(Q4);
SI_macro_rot=Q4t*SI_macro; % Rotating the load

% Angles defining the position of the
% hydrate needle on the aggregate
% Because of symmetry it is enough to ...
    calculate points in the first octant of the ...
    aggregate sphere
for omegait=1:stepsangle
    omega=angle_dis(omegait);
    for psiit=1:stepsangle
        psi=angle_dis(psiit);

        Q4=fun_Q4_bp(omega,psi); ...
            Q4t=transpose(Q4);
        BITZagg=Q4*BITZagg_sph*Q4t; % ...
            Transformation of the stress ...
            concentration tensor to the ...
            Cartesian base

        si_ITZ= BITZagg* ...
            B_agg{acit,wcit,xiit}* ...
            SI_macro_rot; % stress in the ITZ
        eps_ITZ=inv(C_ITZ)*si_ITZ; % Strain in ...
            the ITZ

        % Second-order moments of volumetric ...
            and deviatoric hydrate stresses
        si_hyd_vol2= khyd*sqrt(3*eps_ITZ'* ...
            (diffQ(wcit,xiit).vol *eps_ITZ));
        si_hyd_dev2= muhyd*sqrt(2*eps_ITZ'* ...
            (diffQ(wcit,xiit).dev *eps_ITZ));

        % Drucker-Prager failure criterion
        fDP= si_hyd_dev2/sqrt(2)- alpha_DP* ...
            si_hyd_vol2 / sqrt(3);
        SI_DP_curr=k_DP/fDP; % Current load factor

        % Saving the critical results
        if SI_DP_curr < SI_DP
            SI_DP=SI_DP_curr; % Critical load ...
                factor
            zeni_crit_DP=theta;
            psi_crit_DP=psi;
            omega_crit_DP=omega;
            azi_crit_DP=phi;
            si_hyd_vol2_plot=si_hyd_vol2;
            si_hyd_dev2_plot=si_hyd_dev2;
        end
```

```matlab

                                end
                            end
                        end
                    end

                    % Calculating the elastic limit stress state with
                    % the load factor and saving the results for each ...
                        stress state.
                    r_result(gammait,lodeit)=r*SI_DP*1000; % [MPa]
                    xi_result(gammait,lodeit)=xi*SI_DP*1000; % [MPa]
                    sig1_result(gammait,lodeit)= sig_1 * SI_DP*1000; % [MPa]
                    sig2_result(gammait,lodeit)= sig_2 * SI_DP*1000; % [MPa]
                    sig3_result(gammait,lodeit)= sig_3 * SI_DP*1000; % [MPa]
                    phi_result(gammait,lodeit)=azi_crit_DP;
                    theta_result(gammait,lodeit)=zeni_crit_DP;
                    psi_result(gammait,lodeit)=psi_crit_DP;
                    omega_result(gammait,lodeit)=omega_crit_DP;
                end
            end

            % Saving the results for each concrete mixture
            r_mix{wcit,xiit,acit}=r_result;
            xi_mix{wcit,xiit,acit}=xi_result;
            sig1_mix{wcit,xiit,acit}=sig1_result;
            sig2_mix{wcit,xiit,acit}=sig2_result;
            sig3_mix{wcit,xiit,acit}=sig3_result;
            phi_mix{wcit,xiit,acit}=phi_result;
            theta_mix{wcit,xiit,acit}=theta_result;
            psi_mix{wcit,xiit,acit}=psi_result;
            omega_mix{wcit,xiit,acit}=omega_result;
        end
    end
end
```

Code D.2: Calculation of the elastic limit in Cartesian coordinates for a biaxial stress state

```matlab
%% Phase specific input parameter
number_of_alpha=1;
wc_list=0.5; % Water-to-cement mass ratio
ac_list=3; % Aggregate-to-cement mass ratio
alpha_list=1; % Hydration degree

tolerance = 1e-10;
tolerance_2 = 1e-8;
rho.H2O=1000; rho.hyd=2073; rho.cem=3150; rho.agg=2650; % Densities [kg/m3]
kagg=35.35; muagg=29.91; % Bulk and shear modulus of aggregates [GPa]
```

```
% Initializing precalculation
diffQ(numel(wc_list),number_of_alpha).vol=[];
diffQ(numel(wc_list),number_of_alpha).dev=[];
Chom(numel(ac_list),numel(wc_list),number_of_alpha).hf=[];
Chom(numel(ac_list),numel(wc_list),number_of_alpha).cp=[];

%% Precalculate diffQ and homogenized stiffness tensor for the hydrate ...
    foam and the cement paste Chom
for wcit=1:length(wc_list)
    wc=wc_list(wcit);
    for xiit=1:length(alpha_list)
        xi_p=alpha_list(xiit);
        if isempty(diffQ(wcit,xiit).vol)
            [diffQ(wcit,xiit),Chom(1,wcit,xiit)] = fun_CCR2018_precalc(wc, ...
                xi_p, rho, tolerance, tolerance_2); % see Code D.4
        end
    end
end


%% Hydrate needle parameter
% Mohr-Coulomb
phi_hyd_degree=12; % Friction angle [degree]
c_hyd=0.050; % Cohesion [GPa]
phi_hyd=phi_hyd_degree*pi/180; % Friction angle [rad]
fc_MC=2*c_hyd*cos(phi_hyd)/(1-sin(phi_hyd)); % Strength
Ehyd=29.15786664; % Young's modulus
nuhyd=0.24; % Poisson's ratio
khyd=Ehyd/3/(1-2*nuhyd); % Bulk modulus
muhyd=Ehyd/2/(1+nuhyd); % Shear modulus

% Drucker-Prager (based on Mohr-Coulomb parameters)
alpha_DP=sqrt(3)*fc_MC*tan(phi_hyd)/(3*c_hyd+fc_MC*tan(phi_hyd));
k_DP=c_hyd*alpha_DP/tan(phi_hyd);
fc_DP=3*k_DP/(sqrt(3)-alpha_DP); % Strength


%% Define stress state
% The applied stress state is defined in Cartesian coordinates

beta_1_list=0;
beta_2_list=linspace(0,1,5);


%% Initializing elastic limit calculation

Chom(numel(ac_list),numel(wc_list),numel(alpha_list(1,:))).con=zeros(6);
B_agg=cell(numel(ac_list),numel(wc_list),numel(alpha_list(1,:)));

```

```
phi_result=zeros(1,numel(beta_2_list));
theta_result=zeros(1,numel(beta_2_list));
psi_result=zeros(1,numel(beta_2_list));
omega_result=zeros(1,numel(beta_2_list));

load_factor_list=zeros(1,numel(beta_2_list));



load_factor_mix=cell(length(wc_list),length(alpha_list(1,:)),numel(ac_list));
phi_mix=cell(length(wc_list),length(alpha_list(1,:)),numel(ac_list));
theat_mix=cell(length(wc_list),length(alpha_list(1,:)),numel(ac_list));
psi_mix=cell(length(wc_list),length(alpha_list(1,:)),numel(ac_list));
omega_mix=cell(length(wc_list),length(alpha_list(1,:)),numel(ac_list));


%% Calculation of the elastic limit

% Loop over the concrete mixtures
for wcit=1:length(wc_list)
    wc=wc_list(wcit);
    for xiit=1:length(alpha_list)
        xi_p=alpha_list(xiit);
        for acit=1:numel(ac_list)
            ac=ac_list(acit);

            % Loop over the different stress states
            for beta_2it=1:numel(beta_2_list) % loop over the biaxial ...
                stress states
                beta_2=beta_2_list(beta_2it);

                SI_macro=[-1*beta_1,-1*beta_2,-1,0,0,0]'; % Applied ...
                    macroscopic load in the Cartesian e1,e2,e3 base

                SI_DP=1000; SI_vM=1000; SI_MC=1000; % [GPa] % Initialization

                % Homogenization of the concrete
                Chom(acit,wcit,xiit).hf=Chom(1,wcit,xiit).hf;
                Chom(acit,wcit,xiit).cp=Chom(1,wcit,xiit).cp;
                [Chom(acit,wcit,xiit).con,B_agg{acit,wcit,xiit}] = ...
                    fun_CCR2018_conhom(ac, wc, rho, Chom(1,wcit,xiit).cp, ...
                    kagg, muagg); % see Code D.5

                % First order stress concentration to ITZ
                [~,~,k_ITZ,mu_ITZ]=fun_Enu_from_C( Chom(acit, wcit, ...
                    xiit).cp); % see Code D.9
                C_ITZ=fun_Cfromkmu(k_ITZ,mu_ITZ); see Code D.8
                BITZagg_sph = fun_BITZagg(kagg,k_ITZ,muagg,mu_ITZ); % see ...
                    Code D.6

```

```
% Define angles stepps
stepsangle=45;
angle_dis=0:pi/(2*(stepsangle-1)):pi/2;

% Angles of the hydrate needle in the space
% Because of symmetry it is enough to calculate points in ...
    the hemisphere
for thetait=1:stepsangle
    theta=angle_dis(thetait);
    for phiit=1:stepsangle
        phi=angle_dis(phiit)*2;

        Q4=fun_Q4_bp(phi,theta);
        Q4t=transpose(Q4);
        SI_macro_rot=Q4t*SI_macro; % Rotating the load

        % Angles defining the position of the
        % hydrate needle on the aggregate
        % Because of symmetry it is enough to calculate ...
            points in the first octant of the aggregate sphere
        for omegait=1:stepsangle
            omega=angle_dis(omegait);
            for psiit=1:stepsangle
                psi=angle_dis(psiit);

                Q4=fun_Q4_bp(omega,psi); Q4t=transpose(Q4);
                BITZagg=Q4*BITZagg_sph*Q4t; % ...
                    Transformation of the stress ...
                    concentration tensor to the Cartesian base

                si_ITZ= BITZagg* B_agg{acit,wcit,xiit}* ...
                    SI_macro_rot; % stress in the ITZ
                eps_ITZ=inv(C_ITZ)*si_ITZ; % Strain in the ITZ

                % Second-order moments of volumetric and ...
                    deviatoric hydrate stresses
                si_hyd_vol2= khyd*sqrt(3*eps_ITZ'* ...
                    (diffQ(wcit,xiit).vol *eps_ITZ));
                si_hyd_dev2= muhyd*sqrt(2*eps_ITZ'* ...
                    (diffQ(wcit,xiit).dev *eps_ITZ));

                % Drucker-Prager failure criterion
                fDP= si_hyd_dev2/sqrt(2)- alpha_DP* ...
                    si_hyd_vol2 / sqrt(3);
                SI_DP_curr=k_DP/fDP; % Current load factor

                % Saving the critical results
                if SI_DP_curr < SI_DP
                    SI_DP=SI_DP_curr; % Critical load factor
                    zeni_crit_DP=theta;
```

```
                                    psi_crit_DP=psi;
                                    omega_crit_DP=omega;
                                    azi_crit_DP=phi;
                                    si_hyd_vol2_plot=si_hyd_vol2;
                                    si_hyd_dev2_plot=si_hyd_dev2;
                                end

                            end
                        end
                    end
                end

                % Saving the results for each stress state.
                load_factor_list(beta_2it)=-SI_DP*1000; % [MPa]
                phi_result(beta_2it)=azi_crit_DP;
                theta_result(beta_2it)=zeni_crit_DP;
                psi_result(beta_2it)=psi_crit_DP;
                omega_result(beta_2it)=omega_crit_DP;
            end

            % Saving the results for each concrete mixture
            load_factor_mix{wcit,xiit,acit}=load_factor_list;
            phi_mix{wcit,xiit,acit}=phi_result;
            theta_mix{wcit,xiit,acit}=theta_result;
            psi_mix{wcit,xiit,acit}=psi_result;
            omega_mix{wcit,xiit,acit}=omega_result;
        end
    end
end
```

Code D.3: Plot benchmark concrete Fig. 3.3 and Fig. 3.4

```

% Define colors
color_r_xi_0=rgb('Crimson');
color_r_xi_30=rgb('LawnGreen');
color_r_xi_60=rgb('DodgerBlue');
color_bi=rgb('ForestGreen');
color_dev_max=rgb('DarkOrange');
color_dev_23=rgb('DarkViolet');

% wc_list, xi_list, ac_list, and lode_list are taken over from Code D.1

% beta_2_list is taken over from Code D.2

% Loop over the different mixtures
for wcit=1:length(wc_list)
```

```
    wc=wc_list(wcit);
    for xiit=1:length(xi_list)
        xi_p=xi_list(xiit);
        for acit=1:numel(ac_list)
            ac=ac_list(acit);

            % Lean out results
            r_result=r_mix{wcit,xiit,acit}; % see Code D.1
            xi_result=xi_mix{wcit,xiit,acit}; % see Code D.1
            SI_DP_bi_list=load_factor_mix{wcit,xiit,acit}; % see Code D.2

            % Extrapolate the r and xi to the lode angle 0 and 60
            lode_plot= [0 lode_list pi/3];
            xi_plot= [zeros(numel(r_result(:,1)),1), xi_result , ...
                zeros(numel(r_result(:,1)),1)];
            r_plot= [zeros(numel(r_result(:,1)),1), r_result,  ...
                zeros(numel(r_result(:,1)),1)];
            for rit = 1:numel(r_result(:,1))
                xi_plot(rit,1)= interp1(lode_list, xi_result(rit,:), 0, ...
                    'PCHIP', 'extrap');
                xi_plot(rit,end)= interp1(lode_list, xi_result(rit,:), ...
                    pi/3, 'PCHIP', 'extrap');
                r_plot(rit,1)= interp1(lode_list, r_result(rit,:), 0, ...
                    'PCHIP', 'extrap');
                r_plot(rit,end)= interp1(lode_list, r_result(rit,:), pi/3, ...
                    'PCHIP', 'extrap');
            end

            [tmpind_row,tmpind_col]=find(r_plot>0,1,'last');
            r_plot(tmpind_row+1,:)=0;

            for lodeit = 1:numel(lode_plot)
                xi_plot(tmpind_row+1,lodeit)= ...
                    interp1(r_plot(tmpind_row-5:tmpind_row,lodeit), ...
                    xi_plot(tmpind_row-5:tmpind_row,lodeit), 0, 'PCHIP', ...
                    'extrap');
            end

            % Rotate and mirror the lode angle to get 360 degrees
            mirror=[1,1,1,-1,-1,-1]';
            rotate=[0,2/3*pi,4/3*pi,0,2/3*pi,4/3*pi]';
            lode_360=mirror*lode_plot+rotate;

            % Elastic limits
            fc_uni=SI_DP_bi_list(1);
            fc_bi=SI_DP_bi_list(end);
            fc_hydro=min(xi_plot(:))*sqrt(3)/3;

            % Interpolate between r_plot and xi_plot
            xi_q=0:-1:-500;
```

```
r_q=zeros(numel(xi_q),numel(lode_plot));
for lodeit=1:numel(lode_plot)
    r_q(:,lodeit)= interp1(xi_plot(:,lodeit), ...
        r_plot(:,lodeit), xi_q');
end


%% Cross section along the hydrostatic axis
figure
hold on

% Plot Lode angle = 0
xi_q_0= linspace(max(xi_plot(:,1)), min(xi_plot(:)), 40);
s_0=spline(xi_plot(:,1), r_plot(:,1), xi_q_0);
plot(-xi_q_0, s_0,'linewidth', 1.5,'color', color_r_xi_0)

% Plot Lode angle = 30
[~,indx_lode30] = min(abs(lode_plot-pi/6));
xi_q_30= linspace(max(xi_plot(:,indx_lode30)), ...
    min(xi_plot(:)), 40);
s_30= spline(xi_plot(:,indx_lode30), r_plot(:,indx_lode30), ...
    xi_q_30);
plot(-xi_q_30, s_30, 'color', color_r_xi_30, 'linewidth',1.5)

% Plot Lode angle = 60
xi_q_60= linspace(max(xi_plot(:,end)),min(xi_plot(:)),40);
s_60=spline(xi_plot(:,end),r_plot(:,end),xi_q_60);
plot(-xi_q_60,s_60, 'linewidth',1.5,'color',color_r_xi_60)

% Legend and axis labeling
xlabel('$\xi $ [MPa]')
ylabel('$r$ [MPa]')
legend({'$\theta = 0^{\circ} $', '$\theta = 30^{\circ} $', ...
    '$\theta = 60^{\circ} $'},'Box','on','Location','southwest')
ax = gca;
set(ax,'YAxisLocation','left')
grid on
ylim([0,80])

% Label uniaxial elastic limit
plot(-xi_plot(1,end), r_plot(1,end), 'ko', ...
    'HandleVisibility','off', 'color',color_r_xi_60)
text(-xi_plot(1,end), r_plot(1,end),'$\Sigma_{uni}^{lim}$', ...
    'interpreter','latex', 'VerticalAlignment','bottom')

% Label hydrostatic elastic limit
plot(-xi_plot(end,end), r_plot(end,end), ...
    'k*','HandleVisibility','off')
```

```
            text(-xi_plot(end,end)+5, r_plot(end,end), ...
                '$\Sigma_{hyd}^{lim}$', 'interpreter','latex', ...
                'VerticalAlignment','bottom', 'HorizontalAlignment','left')

            % Label symetric biaxial elastic limit
            plot(-xi_plot(1,1), r_plot(1,1),'ks', ...
                'HandleVisibility','off', 'color',color_r_xi_0)
            text(-xi_plot(1,1)+5, r_plot(1,1), '$\Sigma_{bi}^{lim}$', ...
                'interpreter','latex', 'VerticalAlignment','bottom', ...
                'HorizontalAlignment','left')

            % Set figure size
            set(gca, 'FontSize',10, 'FontName','Times', ...
                'Units','centimeter', 'Position',[1.4,1.2,14,3.5])
            set(gcf, 'Units', 'centimeter', 'PaperPositionMode', ...
                'auto','Position', [0   0 15.9 5]);
            hold off


            %% 3D elastic limit surface
            figure
            hold on

            % Convert cylinder coordinates into Cartesian coordinates
            for ploit = 1:numel(lode_360(:,1))
                x_cat=r_plot.*cos(lode_360(ploit,:));
                y_cat=r_plot.*sin(lode_360(ploit,:));
                % Plot elastic limit surface
                surf(x_cat, y_cat, xi_plot, 'facecolor',rgb('LightGray'), ...
                    'FaceLighting','gouraud', 'edgecolor','none', ...
                    'FaceAlpha',0.85)
            end

            % Plot hydrostatic axis
            plot3([0,0],[0,0],[50,min(xi_plot(:))-50],'k--')

            % plot biaxial cross section
            for ploit = [3,6]
                x_cat=r_plot(1,:).*cos(lode_360(ploit,:));
                y_cat=r_plot(1,:).*sin(lode_360(ploit,:));
                plot3(x_cat, y_cat, xi_plot(1,:), 'color', color_bi, ...
                    'linewidth',2)
            end

            % Plot cross section along the hydrostatic axis at a Lode ...
                angle = 0 degrees
            x_cat=r_plot(:,1).*cos(2*pi()/3);
            y_cat=r_plot(:,1).*sin(2*pi()/3);
            plot3(x_cat, y_cat, xi_plot(:,1), 'color', color_r_xi_0, ...
                'linewidth',2)
```

```

        plot3(x_kat(1),y_kat(1),xi_plot(1,1),'k square','linewidth',2) ...
            % Symmetric biaxial elastic limit

        x_kat=r_plot(:,1).*cos(4*pi()/3);
        y_kat=r_plot(:,1).*sin(4*pi()/3);
        plot3(x_kat(1),y_kat(1),xi_plot(1,1),'k square','linewidth',2) ...
            % Symmetric biaxial elastic limit

        x_kat=r_plot(:,1).*cos(0*pi()/3);
        y_kat=r_plot(:,1).*sin(0*pi()/3);
        plot3(x_kat(1),y_kat(1),xi_plot(1,1),'k square','linewidth',2) ...
            % Symmetric biaxial elastic limit

        % Plot cross section along the hydrostatic axis at a Lode ...
            angle = 30 degrees
        [~,indx_lode30] = min(abs(lode_plot-pi/6));
        x_cat=r_plot(:,indx_lode30).*cos(3*pi()/6);
        y_cat=r_plot(:,indx_lode30).*sin(3*pi()/6);
        plot3(x_cat, y_cat, xi_plot(:,indx_lode30), 'color', ...
            color_r_xi_30, 'linewidth',2)

        % Plot cross section along the hydrostatic axis at a Lode ...
            angle = 60 degrees
        x_cat=r_plot(:,end).*cos(pi()/3);
        y_cat=r_plot(:,end).*sin(pi()/3);
        plot3(x_cat, y_cat, xi_plot(:,end), 'color', color_r_xi_60, ...
            'linewidth',2)

        plot3(x_kat(1),y_kat(1),xi_plot(1,end),'ko','linewidth',1.5) % ...
            Uniaxial elastic limit

        x_kat=r_plot(:,end).*cos(3*pi()/3);
        y_kat=r_plot(:,end).*sin(3*pi()/3);
        plot3(x_kat(1),y_kat(1),xi_plot(1,end),'ko','linewidth',1.5) % ...
            Uniaxial elastic limit

        x_kat=r_plot(:,end).*cos(5*pi()/3);
        y_kat=r_plot(:,end).*sin(5*pi()/3);
        plot3(x_kat(1),y_kat(1),xi_plot(1,end),'ko','linewidth',1.5) % ...
            Uniaxial elastic limit

        % Plot deviatoric plane at xi=xi(r_max)
        [idx_row, ~] = find(r_q==max(r_q));
        indx=idx_row(1);
        xi_at_the_position= xi_q(indx).* ones(length(r_q(1,:)), 1);
        for ploit = 1:numel(lode_360(:,1))
            % Convert into Cartesian coordinates
            x_cat=r_q(indx,:).*cos(lode_360(ploit,:));
            y_cat=r_q(indx,:).*sin(lode_360(ploit,:));
```

```
        plot3(x_cat, y_cat, xi_at_the_position, 'color', ...
            color_dev_max, 'linewidth',2)
    end

    % deviatoric plane at xi = 2/3 xi_max
    val_xi=min(xi_plot(:))*2/3;
    [~,indx] = min(abs(xi_q-val_xi));
    xi_at_the_position= xi_q(indx).* ones(length(r_q(1,:)),1);
    for ploit = 1:numel(lode_360(:,1))
        x_cat=r_q(indx,:).*cos(lode_360(ploit,:));
        y_cat=r_q(indx,:).*sin(lode_360(ploit,:));
        plot3(x_cat, y_cat, xi_at_the_position, 'color', ...
            color_dev_23, 'linewidth',2)
    end

    % Plot Cartesian Axis
    achse.spann= [-max(r_plot(:))-max(r_plot(:)) *1,0,0,0,0,0];
    [achse.xi,achse.r, achse.lode,~,~,~] = ...
        fun_cart_to_haigh(achse.spann); see Code D.10
    scale.spann=[-150,0,0,0,0,0];
    [scale.xi,scale.r,scale.lode,~,~,~] = ...
        fun_cart_to_haigh(scale.spann); see Code D.10
    p_0=[0,0,0];
    achse_1=[achse.r*cos(real(achse.lode)), ...
        achse.r*sin(real(achse.lode)), achse.xi];
    achse_2= [achse.r*cos(real(achse.lode+2*pi/3)), ...
        achse.r*sin(real(achse.lode+2*pi/3)), achse.xi];
    achse_3= [achse.r*cos(real(achse.lode+4*pi/3)), ...
        achse.r*sin(real(achse.lode+4*pi/3)), achse.xi];
    mArrow3(p_0,achse_1);
    text(achse_1(1), achse_1(2), achse_1(3),'  $\Sigma_{1}$', ...
        'FontSize',11);

    mArrow3(p_0,achse_2);
    text(achse_2(1), achse_2(2), achse_2(3),'  $\Sigma_{2}$', ...
        'FontSize',11, 'verticalalignment','bottom');

    mArrow3(p_0,achse_3);
    text(achse_3(1), achse_3(2), achse_3(3),' \hspace{0.2mm} $ ...
        \Sigma_{3}$', 'FontSize',11);

    % Set axis and camera position
    grid on
    camlight
    axis off
    axis equal
    campos([1785.00498042272 1555.49888531135 1263.48472494576]);
    camup(-achse_3);
    camtarget([-11.5245746347532 -5.24438981834146 ...
        -243.473208398794]);
```

```
        camva(9.24455604601039);
        light('Position',[163.139519034882 2745.46095812313 ...
            2373.80086306804])

        % Set figure size
        set(gca, 'FontSize',10,'FontName', 'Times', ...
            'Units','centimeter', 'Position',[1,-8.0,20,20])
        set(gcf, 'Units','centimeter', 'PaperPositionMode','auto', ...
            'Position',[0   0 15 9]);

        hold off


        %% Deviatoric plane
        figure;

        % deviatoric plane at xi = 2/3 xi_max
        val_xi=min(xi_plot(:))*2/3;
        [minValue,indx] = min(abs(xi_q-val_xi));
        xi2= polarplot(lode_360(1,:), r_q(indx,:), 'linewidth',1.5, ...
            'color',color_dev_23);
        hold on
        for ploit = 2:numel(lode_360(:,1))
            polarplot(lode_360(ploit,:), r_q(indx,:), ...
                'HandleVisibility','off', ...
                'linewidth',1.5,'color',color_dev_23)
        end

        % Plot deviatoric plane at xi=xi(r_max)
        [idx_row, idx_column] = find(r_q==max(r_q));
        indx=idx_row(1);
        xirmax= polarplot(lode_360(1,:), r_q(indx,:), 'linewidth',1.5, ...
            'color', color_dev_max);
        hold on
        for ploit = 2:numel(lode_360(:,1))
            polarplot(lode_360(ploit,:), r_q(indx,:), ...
                'HandleVisibility','off', 'linewidth',1.5,'color', ...
                color_dev_max)
        end

        % Label symmetric biaxial compression points
        polarplot(lode_360(1,1), r_q(indx,1),'bs', 'color', ...
            color_dev_max);
        text(lode_360(1,1), r_q(indx,1), '$\Sigma_{bi}^{lim}$', ...
            'interpreter','latex', 'VerticalAlignment','bottom', ...
            'HorizontalAlignment','right')

        polarplot(lode_360(2,1), r_q(indx,1),'bs', 'color', ...
            color_dev_max);
```

```
        text(lode_360(2,1), r_q(indx,1),'$\Sigma_{bi}^{lim}$', ...
            'interpreter','latex', 'VerticalAlignment','bottom', ...
            'HorizontalAlignment','left')

        polarplot(lode_360(3,1), r_q(indx,1),'bs', 'color',color_dev_max);
        text(lode_360(3,1), r_q(indx,1),'$\Sigma_{bi}^{lim}$', ...
            'interpreter','latex', 'VerticalAlignment','bottom', ...
            'HorizontalAlignment','right')

        % Principal stress axes
        myarrow([0,pi/3],[0,max(r_q(:))+10])
        myarrow([0,pi],[0,+max(r_q(:))+10])
        myarrow([0,5*pi/3],[0,max(r_q(:))+10])

        polarplot([0,0], [0,+max(r_q(:))+10], ...
            'k--','HandleVisibility', 'off','linewidth',0.1)
        polarplot([0,2*pi/3], [0,+max(r_q(:))+10], ...
            'k--','HandleVisibility', 'off')
        polarplot([0,4*pi/3], [0,+max(r_q(:))+10], ...
            'k--','HandleVisibility', 'off')

        % Ticks
        thetaticks( [0 30 60 90 120 150 180 210 240 270 300 330])
        thetaticklabels({'$0$', '$\pi/6$', '$\Sigma_{3}$', '$\pi/2$', ...
            '$2\pi/3$', '$5\pi/6$', '$\Sigma_{1}$',  '$7\pi/6$' ...
            ,'$4\pi/3$', '$3\pi/2$', '$\Sigma_{2}$',  '$11\pi/6$'})

        % Legend
        legend({'$\xi=2/3 \, \xi_{max}$', ...
            '$\xi=\xi(\Sigma_{bi}^{lim})$'}, 'Location','northoutside', ...
            'Box','on')

        % Set axis
        ax=gca;
        ax.ThetaZeroLocation = 'top';
        ax.GridLineStyle = '--';
        ax.ThetaAxisUnits = 'radians';
        ax.ThetaDir = 'clockwise';
        rlim([0,max(r_q(:))+10])
        set(ax,'TickLabelInterpreter','latex')

        % Set figure size
        set(gca, 'FontSize',10,'FontName', ...
            'Times','Units','centimeter', 'Position',[1,0.4,6.5,7.0])
        set(gcf, 'Units','centimeter', 'PaperPositionMode','auto', ...
            'Position',[0   0 8.3 9.0]);


        %% Biaxial plane
        figure
```

```
            hold on; grid on

            % plot biaxial plane
            xq=linspace(0,min(SI_DP_bi_list),100);
            s = spline(beta_2_list.*SI_DP_bi_list, SI_DP_bi_list, xq);
            plot(-s,-xq,'-','linewidth',1.5,'color',color_bi)
            plot(-xq,-s,'-','linewidth',1.5,'color',color_bi)

            % Label symetric biaxial elastic limit
            plot(-SI_DP_bi_list(end), ...
                -beta_2_list(end).*SI_DP_bi_list(end), 'ks', 'color',color_bi)
            text(-SI_DP_bi_list(end), ...
                -beta_2_list(end).*SI_DP_bi_list(end)+2, ...
                '$\Sigma_{bi}^{lim}$', 'interpreter','latex', ...
                'VerticalAlignment','bottom')
            % Label uniaxial elastic limit
            plot(-SI_DP_bi_list(1), -beta_2_list(1).*SI_DP_bi_list(1), ...
                'ko', 'color',color_bi)
            text(-SI_DP_bi_list(1)+2, -beta_2_list(1).*SI_DP_bi_list(1)+1, ...
                '$\Sigma_{uni}^{lim}$', 'interpreter','latex', ...
                'VerticalAlignment','bottom', 'HorizontalAlignment','left')
            plot(-beta_2_list(1).*(SI_DP_bi_list(1)), -SI_DP_bi_list(1), ...
                'ko', 'color',color_bi)
            text(-beta_2_list(1).*(SI_DP_bi_list(1))+2, ...
                -SI_DP_bi_list(1)+2, '$\Sigma_{uni}^{lim}$', ...
                'interpreter','latex', 'VerticalAlignment','bottom', ...
                'HorizontalAlignment','left')

            % Set axis
            axis square
            xlim([0,-fc_bi+10])
            ylim([0,-fc_bi+10])
            xlabel('$\Sigma_{2}$ [MPa]','interpreter','latex')
            ylabel('$\Sigma_{3}$ [MPa]','interpreter','latex')
            hold off


            % Set figure size
            set(gca, 'FontSize',10, 'FontName','Times', ...
                'Units','centimeter', 'Position',[1.4,1.2,6.0,6.0])
            set(gcf, 'Units','centimeter', 'PaperPositionMode','auto', ...
                'Position',[0   0 8.3 8.3]);

        end
    end
end
```

Code D.4: Precalculation of the difference quotients and the homogenized stiffness tensor of the hydrate foam and the cement paste

```
function [diffQ,Chom] = fun_CCR2018_precalc(wc,xi,rho,tolerance,tolerance_2)

    %% General
    % Load unity tensors and stroud points
    stroud_points

    % Standard phase stiffness
    % Cement clinker
    Eclin=139.9;
    nuclin=0.3;
    kclin=Eclin/3/(1-2*nuclin);
    muclin=Eclin/2/(1+nuclin);
    Cclin=3*kclin*J+2*muclin*K;

    % Needle-shaped hydrates
    Ehyd=29.15786664;
    nuhyd=0.24;
    khyd=Ehyd/3/(1-2*nuhyd);
    muhyd=Ehyd/2/(1+nuhyd);
    Chyd=3*khyd*J+2*muhyd*K;

    % Pores
    Cp=zeros(6,6);

    % Numerical values for strength approximation
    fapp=0.001;
    muhyddiff=(1+fapp)*muhyd;
    khyddiff=(1+fapp)*khyd;
    fhyddiff=fapp/5;

    %% Volume fractions
    % Powers model -> cement paste volumes
    xiult=wc/0.42;
    if xi>xiult;
        xi=xiult;
        disp(['ultimate hydration degree,' num2str(xiult),' is reached'])
    end
    fcem_PA = (1-xi)/(1+rho.cem/rho.H2O*wc);
    fhyd_PA = 1.42*rho.cem*xi/(rho.hyd*(1+rho.cem/rho.H2O*wc));
    fH2O_PA = max(0,rho.cem*(wc-0.42*xi)/(rho.H2O*(1+rho.cem/rho.H2O*wc)));
    fair_PA = 1-fcem_PA-fH2O_PA-fhyd_PA;

    fcem_cp=fcem_PA;
    fhyd_cp=fhyd_PA;

    % Hydrate foam volumes
```

```
    fhf_cp=fhyd_cp+fH2O_PA+fair_PA;
    fpor_hf=(fH2O_PA+fair_PA)./fhf_cp;
    fhyd_hf=fhyd_cp./fhf_cp;


    %% Elasticity hydrate foam
    C0 = fhyd_hf*Chyd;
    deviation=1;

    while deviation > tolerance
        % Spherical pores
        P_p=fun_P_sphere_iso(C0);
        Ainf_p=inv(I+P_p*(Cp-C0));

        % Acicular hydrates, orientated isotropically in all space directions
        Ainf_hyd=fun_Ainf_needle_iso(Chyd,C0); % see Code D.7

        % Strain concentration tensors
        EEinfty_hf=inv(fpor_hf*Ainf_p + fhyd_hf*Ainf_hyd);
        A_p=Ainf_p*EEinfty_hf;
        A_hyd=Ainf_hyd*EEinfty_hf;

        % Homogenized stiffness - SELF CONSISTENT
        Chom_hf=fhyd_hf*Chyd*A_hyd;

        % Update
        C0_old=C0;
        C0=Chom_hf;
        deviation=abs(norm(C0-C0_old)/norm(C0));
    end


    %% Elasticity cement paste
    C0=Chom_hf;

    % Spherical clinkers, SCMs, and inert fillers
    P_sph=fun_P_sphere_iso(C0);
    Ainf_cem=inv(I+P_sph*(Cclin-C0));
    Ainf_hf=I;

    % Strain concentration tensors
    EEinfty_cp=inv(fcem_cp*Ainf_cem + fhf_cp*Ainf_hf);
    A_cem=Ainf_cem*EEinfty_cp;
    A_hf=Ainf_hf*EEinfty_cp;

    % Homogenized stiffness (MORI-TANAKA)
    Chom_cp=fcem_cp*Cclin*A_cem + fhf_cp*Chom_hf*A_hf;


    %% 2nd order deviator hydrate foam
```

```
C0 = Chom_hf;
Chyd_diff=3*khyd*J+2*muhyddiff*K;

deviation=1;
countermark=0;
while deviation > tolerance_2 && countermark<10
    disp(['DEV: error=',num2str(deviation,6),' > ...
        tolerance=',num2str(tolerance_2),'  ...
        C1111=',num2str(C0(1,1),10),'  C3333=',num2str(C0(3,3),10)])
    countermark=countermark+1;
    % spherical pores
    P_p=P_isotrans_sph(C0);
    Ainf_p=inv(I+P_p*(Cp-C0));

    % Acicular hydrates, orientated isotropically in all space directions
    sumAinf_hyd=zeros(6,6);
    for i=1:15
        % Transformation matrices
        azi=stroud_azi(i); zeni=stroud_zeni(i);
        Q4=fun_Q4_bp(azi,zeni); Q4t=transpose(Q4);

        % Transformation of stiffness components in negative needle ...
            orientation
        C0_aniso=Q4*C0*Q4t;
        P_hyd_i_e3=fun_P_ellipsoid_transiso(C0_aniso,1,1e-20);
        % Transformation back into needle orientation
        P_hyd_i=(Q4t * P_hyd_i_e3 * Q4);

        % Strain concentration tensors in 15 directions + sum
        Ainf_hyd_i=inv(I+P_hyd_i*(Chyd-C0));
        sumAinf_hyd=sumAinf_hyd+Ainf_hyd_i;
    end
    sumAinf_hyd=1/15*sumAinf_hyd;

    % Acicular hydrate with larger mu, orientated in e3
    P_hyd_e3=fun_P_ellipsoid_transiso(C0,1,1e-20);
    Ainf_hyd_diff=inv(I+P_hyd_e3*(Chyd_diff-C0));
    Ainf_hyd_minus=inv(I+P_hyd_e3*(Chyd-C0));

    % Strain concentration tensors
    EEinfty_hf=inv(fpor_hf*Ainf_p + fhyd_hf*sumAinf_hyd + ...
        fhyddiff*Ainf_hyd_diff - fhyddiff*Ainf_hyd_minus);
    A_p=Ainf_p*EEinfty_hf;
    A_hyd=sumAinf_hyd*EEinfty_hf;
    A_hyd_diff=Ainf_hyd_diff*EEinfty_hf;
    A_hyd_minus=Ainf_hyd_minus*EEinfty_hf;

    % Homogenized stiffness - SELF CONSISTENT
    Chom_hf_dev_transiso=fhyd_hf*Chyd*A_hyd + ...
        fhyddiff*Chyd_diff*A_hyd_diff - fhyddiff*Chyd*A_hyd_minus;
```

```

        % Update
        C0_old=C0;
        C0=Chom_hf_dev_transiso;
        deviation=abs(norm(C0-C0_old)/norm(C0));
    end

    %% 2nd order deviator CEMENT PASTE
    C0=Chom_hf_dev_transiso;

    % Spherical clinkers, SCMs, and inert fillers
    P_sph=P_isotrans_sph(C0);
    Ainf_cem=inv(I+P_sph*(Cclin-C0));
    Ainf_hf=I;

    % Strain concentration tensors
    EEinfty_cp_dev_transiso=inv(fcem_cp*Ainf_cem + fhf_cp*Ainf_hf);
    A_cem_dev_transiso=Ainf_cem*EEinfty_cp_dev_transiso;
    A_hf_dev_transiso=Ainf_hf*EEinfty_cp_dev_transiso;

    % Homogenized stiffness (MORI-TANAKA)
    Chom_cp_dev_transiso=fcem_cp*Cclin*A_cem_dev_transiso + ...
        fhf_cp*Chom_hf_dev_transiso*A_hf_dev_transiso;

    %% 2nd order volumetric part HYDRATE FOAM
    C0 = Chom_hf;
    Chyd_diff=3*khyddiff*J+2*muhyd*K;

    deviation=1;
    countermark=0;
    while deviation > tolerance_2 && countermark<8
        disp(['VOL: error=',num2str(deviation,6),' > ...
            tolerance=',num2str(tolerance_2),'  ...
            C1111=',num2str(C0(1,1),10),'  C3333=',num2str(C0(3,3),10)])
        countermark=countermark+1;
        % Spherical pores
        P_p=P_isotrans_sph(C0);
        Ainf_p=inv(I+P_p*(Cp-C0));

        % Acicular hydrates, orientated isotropically in all space directions
        sumAinf_hyd=zeros(6,6);
        for i=1:15
            % Transformation matrices
            azi=stroud_azi(i); zeni=stroud_zeni(i);
            Q4=fun_Q4_bp(azi,zeni); Q4t=transpose(Q4);

            % Transformation of stiffness components in negative needle ...
                orientation
            C0_aniso=Q4*C0*Q4t;
            P_hyd_i_e3=fun_P_ellipsoid_transiso(C0_aniso,1,1e-20);
```

```
        % Transformation back into needle orientation
        P_hyd_i=(Q4t * P_hyd_i_e3 * Q4);

        % Strain concentration tensors in 15 directions + sum
        Ainf_hyd_i=inv(I+P_hyd_i*(Chyd-C0));
        sumAinf_hyd=sumAinf_hyd+Ainf_hyd_i;
    end
    sumAinf_hyd=1/15*sumAinf_hyd;

    % Acicular hydrate with larger k, orientated in e3
    P_hyd_e3=fun_P_ellipsoid_transiso(C0,1,1e-20);
    Ainf_hyd_diff=inv(I+P_hyd_e3*(Chyd_diff-C0));
    Ainf_hyd_minus=inv(I+P_hyd_e3*(Chyd-C0));

    % Strain concentration tensors
    EEinfty_hf=inv(fpor_hf*Ainf_p + fhyd_hf*sumAinf_hyd + ...
        fhyddiff*Ainf_hyd_diff - fhyddiff*Ainf_hyd_minus);
    A_p=Ainf_p*EEinfty_hf;
    A_hyd=sumAinf_hyd*EEinfty_hf;
    A_hyd_diff=Ainf_hyd_diff*EEinfty_hf;
    A_hyd_minus=Ainf_hyd_minus*EEinfty_hf;

    % Homogenized stiffness - SELF CONSISTENT
    Chom_hf_vol_transiso=fhyd_hf*Chyd*A_hyd + ...
        fhyddiff*Chyd_diff*A_hyd_diff - fhyddiff*Chyd*A_hyd_minus;

    % Update
    C0_old=C0;
    C0=Chom_hf_vol_transiso;
    deviation=abs(norm(C0-C0_old)/norm(C0));
end

%% 2nd order volumetric part CEMENT PASTE
C0=Chom_hf_vol_transiso;

% Spherical clinkers, SCMs, and inert fillers
P_sph=P_isotrans_sph(C0);
Ainf_cem=inv(I+P_sph*(Cclin-C0));
Ainf_hf=I;

% Strain concentration tensors
EEinfty_cp_vol_transiso=inv(fcem_cp*Ainf_cem + fhf_cp*Ainf_hf);
A_cem_vol_transiso=Ainf_cem*EEinfty_cp_vol_transiso;
A_hf_vol_transiso=Ainf_hf*EEinfty_cp_vol_transiso;

% Homogenized stiffness (MORI-TANAKA)
Chom_cp_vol_transiso=fcem_cp*Cclin*A_cem_vol_transiso + ...
    fhf_cp*Chom_hf_vol_transiso*A_hf_vol_transiso;
```

```
    %% Difference Quotients
    diffQ.vol=1/(fapp*khyd) * (Chom_cp_vol_transiso-Chom_cp) / ...
        (fhyddiff*fhf_cp); % Attention: volume fraction has been multiplied ...
        already
    diffQ.dev=1/(fapp*muhyd) * (Chom_cp_dev_transiso-Chom_cp) / ...
        (fhyddiff*fhf_cp);

    %% Stiffness
    Chom.hf=Chom_hf;
    Chom.cp=Chom_cp;

end
```

Code D.5: Homogenization of the concrete

```
function [Chom_mor,B_agg] = fun_CCR2018_conhom(ac,wc,rho,Chom_cp,kagg,muagg)
    %% Elasticity mortar/concrete

    stroud_points

    % phase stiffness
    Cagg=3*kagg*J+2*muagg*K; % Aggregates
    Cp=zeros(6,6); % Pores

    % Mortar-related volumes
    fq_mor=(ac/rho.agg)/(1/rho.cem+wc/rho.H2O+ac/rho.agg);
    fcp_mor=1-fq_mor;
    fa_mor=0;

    % Stiffness of matrix in Eshelby problem
    C0=Chom_cp;

    % Spherical clinkers, SCMs, and inert fillers
    P_sph=fun_P_sphere_iso(C0);
    Ainf_q=inv(I+P_sph*(Cagg-C0));
    Ainf_por=inv(I+P_sph*(Cp-C0));
    Ainf_cp=I;

    % Strain concentration tensors
    EEinfty_mor=inv(fcp_mor*Ainf_cp + fq_mor*Ainf_q + fa_mor*Ainf_por);
    A_q=Ainf_q*EEinfty_mor;
    A_cp=Ainf_cp*EEinfty_mor;
    A_por=Ainf_por*EEinfty_mor;

    % Homogenized stiffness (MORI-TANAKA)
    Chom_mor=fcp_mor*Chom_cp*A_cp + fq_mor*Cagg*A_q;

```

```
    % Stress concentration tensor
    B_agg=Cagg*A_q*inv(Chom_mor);

end
```

Code D.6: Stress concentration to ITZ

```
    function [ BITZsand_sph ] = fun_BITZagg(kagg,kITZ,muagg,muITZ)
    %fun_BITZagg Stress concentration tensor to ITZ
    %   calculates the spherical components of the 4th order stress ...
        concentration tensor
    %   BITZagg in the psi, omega, r-base for downscaling aggregate ...
        stresses to
    %   ITZ stresses; all phases are isotropic, spherical aggregates, perfect
    %   bond-related continuity conditions

    deltaITZsand= kagg*muagg*(3*kITZ+4*muITZ);

    BITZsandrrrr= 1.0;
    BITZsandpppp= muITZ*(3*kagg*kITZ+2*kagg*muITZ+2*kITZ*muagg)/deltaITZsand;
    BITZsandoooo= BITZsandpppp;
    BITZsandppoo= 2*muITZ*(kITZ*muagg-kagg*muITZ)/deltaITZsand;
    BITZsandoopp= BITZsandppoo;
    BITZsandoorr= ...
        (3*kagg*kITZ*(muagg-muITZ)-2*muagg*muITZ*(kagg-kITZ))/deltaITZsand;
    BITZsandoorr= BITZsandoorr;
    BITZsandroro= 0.5;
    BITZsandroro= 0.5;
    BITZsandpopo= muITZ/(2*muagg);

    BITZsand_sph= [BITZsandpppp, BITZsandppoo, BITZsandoorr, 0., 0., 0.;...
    BITZsandoopp, BITZsandoooo, BITZsandoorr, 0., 0., 0.;...
    0., 0., BITZsandrrrr, 0., 0., 0.;...
    0., 0., 0., 2*BITZsandroro, 0., 0.;...
    0., 0., 0., 0., 2*BITZsandroro, 0.;...
    0., 0., 0., 0., 0., 2*BITZsandpopo];

    end
```

Code D.7: Auxiliary tensor for the strain concentration tensor of the hydrate needle

```
    function[Ainfneedle]=fun_Ainf_needle_iso(Cinc,Cinf)

    % Function for computation of Ainf for cylindric isotropic inclusions
```

```
% orientated in all space directions, embedded in isotropic matrix ...
    material
%
%-----------------------------------------------------------------------
% INPUT: inclusion stiffness tensor Cinc (isotropic)
%        infinite matrix stiffness tensor Cinf (isotropic)
%
% OUTPUT: Auxiliary tensor Ainfneedle
%
%-----------------------------------------------------------------------
%

% Computation of elastic constants of matrix material
muinc=0.5*Cinc(6,6);
kinc=Cinc(1,1)-4/3*0.5*Cinc(6,6);

muinf=0.5*Cinf(6,6);
kinf=Cinf(1,1)-4/3*0.5*Cinf(6,6);

Avolinf_needle = (1/3)*(3*kinf+muinc+3*muinf)/(3*kinc+muinc+3*muinf);
Adevinf_needle = (1/10)*(9*kinc*muinc^2*kinf+ 84*kinf*muinf^3+ ...
    64*muinf^4+21*kinc*muinc^2*muinf+ 81*kinc*kinf*muinf^2+ ...
    120*kinf*muinc*muinf^2+ 63*kinc*muinf^3+ 184*muinc*muinf^3+ ...
    90*kinf*muinf*kinc*muinc+ 36*kinf*muinf*muinc^2+ ...
    156*kinc*muinc*muinf^2+ 72*muinc^2*muinf^2)/ ...
    ((muinf+muinc)*(3*kinf*muinc+ 7*muinf*muinc+3*kinf*muinf+muinf^2)* ...
    (3*kinc+muinc+3*muinf));

I=  [1 0 0 0 0 0;...
0 1 0 0 0 0;...
0 0 1 0 0 0;...
0 0 0 1 0 0;...
0 0 0 0 1 0;...
0 0 0 0 0 1];

J=  [1/3 1/3 1/3 0 0 0;...
1/3 1/3 1/3 0 0 0;...
1/3 1/3 1/3 0 0 0;...
0   0   0   0 0 0;...
0   0   0   0 0 0;...
0   0   0   0 0 0];

K=I-J;

Ainfneedle=3*Avolinf_needle*J+2*Adevinf_needle*K;
end
```

Code D.8: Calculate isotropic elastic stiffness tensor from bulk and shear modulus

```
function[C]=fun_CfromEnu(k,mu)
% C = fun_CfromEnu(E,nu) returns the isotropic elastic stiffness ...
    tensor of
% a material with bulk modulus k and shear modulus mu
%-----------------------------------------------------------------------
% INPUT: k  ... bulk modulus ->scalar
%       mu ... Shear modulus ->scalar
% OUTPUT: C ... stiffness tensor ->4th tensor
%-----------------------------------------------------------------------

I=[1 0 0 0 0 0;...
0 1 0 0 0 0;...
0 0 1 0 0 0;...
0 0 0 1 0 0;...
0 0 0 0 1 0;...
0 0 0 0 0 1];

Ivol=[1/3 1/3 1/3 0 0 0;...
1/3 1/3 1/3 0 0 0;...
1/3 1/3 1/3 0 0 0;...
0   0   0   0 0 0;...
0   0   0   0 0 0;...
0   0   0   0 0 0];

Idev=I-Ivol;

C=3*k*Ivol+2*mu*Idev;
end
```

Code D.9: Calculation of Young's modulus, Poisson's ratio, bulk and shear modulus from the stiffness tensor

```
function [E,nu,k,mu] = fun_Enu_from_C(C)
    %Calculate Young's modulus (E) and Poisson's ratio (nu), bulk  (k) and
    %shear modulus (mu) from stiffness tensor (C)

    % Verify input
    if ~isequal(size(C), [6,6])
    error('dimension of matrix must be 6x6')
    end

    % Lame constants
    la=C(1,2);
    mu=C(4,4)/2;

```

```
    % Transition
    k=la+2/3*mu;
    nu = (3*k-2*mu)/(6*k+2*mu);
    E = 9*k*mu/(3*k+mu);
end
```

Code D.10: Convert stress tensor in Cartesian coordinates to Haigh-Westergaard coordinates

```
    function [xi,r,lode_rad,sig,J_2,J_3] = fun_cart_to_haigh(spann_kelv_mand)
    % Convert stress state in Cartesian coordinate system
    % into Haigh-Westergaard coordinate system

    % Stress tensor
    sig=[spann_kelv_mand(1), spann_kelv_mand(6)/sqrt(2), ...
        spann_kelv_mand(5)/sqrt(2);
    spann_kelv_mand(6)/sqrt(2), spann_kelv_mand(2), ...
        spann_kelv_mand(4)/sqrt(2);
    spann_kelv_mand(5)/sqrt(2), spann_kelv_mand(4)/sqrt(2), ...
        spann_kelv_mand(3)];

    % Auxiliary values
    aux_sig_1=[sig(2,2),sig(2,3);...
    sig(3,2),sig(3,3)];
    aux_sig_2=[sig(1,1),sig(1,3);...
    sig(3,1),sig(3,3)];
    aux_sig_3=[sig(1,1),sig(1,2);...
    sig(2,1),sig(2,2)];

    % Invariants of the stress tensor
    I_1=sig(1,1)+sig(2,2)+sig(3,3);
    I_2=det(aux_sig_1)+det(aux_sig_2)+det(aux_sig_3);
    I_3=det(sig);

    % Invariants of the stress deviator
    J_2=((I_1)^2)/3-I_2;
    J_3=I_3-I_1*I_2/3+2*I_1^3/27;

    %Haigh-Westergaard coordinates
    xi=I_1/sqrt(3);
    r=sqrt(2*J_2);
    lode_rad=1/3*acos(3*sqrt(3)/2*J_3/(sqrt(J_2^3))); % in rad

    end
```

Code D.11: Convert Haigh-Westergaard coordinates to principal stresses in a Cartesian coordinates

```
function [sig_1,sig_2,sig_3] = ...
    fun_haigh_westergaard_to_cartesian(xi,r,lode)
% Convert stress state in Haigh-Westergaard
% Coordinate system into Cartesian coordinate system

% Invariants of the stress deviator
J_2=r^2/2;
J_3=cos(3*lode)*2/(3*sqrt(3))*sqrt(J_2^3);

% Invariants of the stress tensor
I_1=xi*sqrt(3);
I_2=I_1^2/3-J_2;
I_3=J_3+I_1*I_2/3-2*I_1^3/27;

% Auxiliary values
h_1=I_1^2-3*I_2;
h_frac=asin((2*I_1^3-9*I_1*I_2+27*I_3)/(2*(h_1)^(3/2)))/3;

% Principal stresses in a Cartesian coordinate system
sig_1=(sqrt(h_1)*cos(h_frac+pi/6)+sqrt(3*h_1*(sin(h_frac+pi/6))^2)+I_1)/3;
sig_2=(sqrt(h_1)*cos(h_frac+pi/6)-sqrt(3*h_1*(sin(h_frac+pi/6))^2)+I_1)/3;
sig_3=-(2*sqrt(h_1)*cos(h_frac-pi/6)-I_1)/3;

end
```